



NRL/MR/6410--06-8976

Blast Mitigation by Water Mist

(3) Mitigation of Confined and Unconfined Blasts

D. SCHWER

K. KAILASANATH

Center for Reactive Flow and Dynamical Systems

Laboratory for Computational Physics and Fluid Dynamics

July 14, 2006

REPORT DOCUMENTATION PAGE				Form Approved OMB No. 0704-0188	
Public reporting burden for this collection of information is estimated to average 1 hour per response, including the time for reviewing instructions, searching existing data sources, gathering and maintaining the data needed, and completing and reviewing this collection of information. Send comments regarding this burden estimate or any other aspect of this collection of information, including suggestions for reducing this burden to Department of Defense, Washington Headquarters Services, Directorate for Information Operations and Reports (0704-0188), 1215 Jefferson Davis Highway, Suite 1204, Arlington, VA 22202-4302. Respondents should be aware that notwithstanding any other provision of law, no person shall be subject to any penalty for failing to comply with a collection of information if it does not display a currently valid OMB control number. PLEASE DO NOT RETURN YOUR FORM TO THE ABOVE ADDRESS.					
1. REPORT DATE (DD-MM-YYYY) 14-07-2006		2. REPORT TYPE Memorandum Report		3. DATES COVERED (From - To)	
4. TITLE AND SUBTITLE Blast Mitigation by Water Mist (3) Mitigation of Confined and Unconfined Blasts				5a. CONTRACT NUMBER	
				5b. GRANT NUMBER 64-8804-A-5	
				5c. PROGRAM ELEMENT NUMBER	
6. AUTHOR(S) D. Schwer and K. Kailasanath				5d. PROJECT NUMBER	
				5e. TASK NUMBER	
				5f. WORK UNIT NUMBER	
7. PERFORMING ORGANIZATION NAME(S) AND ADDRESS(ES) Naval Research Laboratory 4555 Overlook Avenue, SW Washington, DC 20375-5320				8. PERFORMING ORGANIZATION REPORT NUMBER NRL/MR/6410--06-8976	
9. SPONSORING / MONITORING AGENCY NAME(S) AND ADDRESS(ES)				10. SPONSOR / MONITOR'S ACRONYM(S)	
				11. SPONSOR / MONITOR'S REPORT NUMBER(S)	
12. DISTRIBUTION / AVAILABILITY STATEMENT Approved for public release; distribution is unlimited.					
13. SUPPLEMENTARY NOTES					
14. ABSTRACT This is the third in a series of reports focusing on numerical simulations of blasts and blast mitigation. This report uses the models developed in the first two to specifically examine the effect of water mists consisting of sub-50-micron droplets on blast shock-fronts and the development of quasi-static overpressure in enclosed spaces. In unconfined blasts, results showed that the water mist does not directly suppress the secondary reactions. Mitigation of the shock-front is accomplished mainly through momentum extraction and not vaporization. Quantitative results determined the exact effect of 5 to 50 micron sized droplets on the shock-front. Droplet size was found to play a secondary role compared to mass loading. Smaller droplets were less effective close to the explosive, while further downstream, the optimum droplet size depended on mass loading. The total amount of water mass between the observer and explosive was the most important factor in determining the amount of mitigation seen by the observer. Simulations were also conducted to determine the effectiveness of water mist to mitigate quasi-static pressure build-up in enclosures. Comparisons with experiments conducted at NSWC were used to validate the models and showed that the models could predict the overall mitigation efficiency to within a few percent. Absolute values of the simulation quasi-static overpressure tended to be slightly higher than experimental values, most likely because various loss mechanisms (incomplete combustion, absorption of energy by walls, and venting) were not incorporated into the model. Results also suggested that multi-dimensional simulations were required compared with simple thermodynamic and one-dimensional computations. Finally, additional needed computational work is summarized in the report. Many of these improvements are implemented and are currently being tested, and will help substantially in simulating blast mitigation scenarios of interest to the Navy and DoD.					
15. SUBJECT TERMS Blast mitigation Water-mist suppression Explosions Damage control Shock suppression Modeling and simulation					
16. SECURITY CLASSIFICATION OF:			17. LIMITATION OF ABSTRACT UL	18. NUMBER OF PAGES 44	19a. NAME OF RESPONSIBLE PERSON Douglas Schwer
a. REPORT Unclassified	b. ABSTRACT Unclassified	c. THIS PAGE Unclassified			19b. TELEPHONE NUMBER (include area code) (202) 767-3615

Blast Mitigation by Water Mist
(3) Mitigation of Confined and Unconfined Blasts

Table of Contents

1.	Introduction
2.	Numerical Model and Solution Procedure
2.1	Gas-phase Model
2.2	Dispersed-phase Model
2.3	Property Evaluation for Blast Mitigation Models
2.4	Solution Procedure
2.5	Wall Boundary Conditions for the Water Mist
3.	Blast Mitigation using Water Mist
4.	Mitigation of the Shock-Front
5.	Mitigation of Quasi-Static Pressure
6.	Computations in Support of Indian Head Experiments
6.1	Pressure Trace Characteristics
6.2	Quasi-static Pressure Characteristics
7.	Challenges
7.1	Non-TNT Explosives and Improved Explosive Detonation
7.2	Improved Droplet Modeling
7.3	Complex Three-Dimensional Geometries with VCE/SS
7.4	Parallel Adaptive Mesh Refinement using PARAMESH
7.5	Fluid-Structure Interaction
8.	Conclusions
	References
A.	Explosive Decomposition

List of Tables

1. Predicted front shock overpressure and quasi-static overpressure. Scaled weight assumes temperature of 298 K and pressure of 1.013 bar for tests.
2. Quasi-static pressure results for Indian Head experiments and simulations at NRL. QSP1 is averaged from $t=0$ to $t=0.05$ seconds, QSP2 is averaged from $t=0.05$ to $t=0.10$ seconds, and QSP3 is averaged from $t=0.00$ to 0.10 seconds. Quasi-static pressure is in psig. Experimental data from Bailey [15].
3. Water-mist effectiveness, calculated by taking the difference in the quasi-static overpressure divided by the unmitigated overpressure.

List of Figures

1. Example of Eulerian treatment of two independent streams. As the streams in (a) come together, they will merge into one large stream with one momentum (b). For very dispersed streams, this is not physically accurate because the streams will tend to pass through each other.
2. Number density as a stream of droplets hit a wall. As it is hitting the wall, droplets will be reflected and reverse in direction. This is difficult for an Eulerian treatment of droplets to reproduce accurately.
3. Temperature (a) and pressure (b) for axisymmetric explosion of 2.12 kg TNT, 1 ms after detonation. Maximum temperature is 2100 K, maximum pressure is 9.1 bar.
4. Magnitude of the gradient of the temperature for an axisymmetric explosion of 2.12 kg TNT. Temperature gradient is saturated at 250 K/cm. Domain length and radius is 200 cm.
5. Gradient of pressure, water mist, and CO concentration for a blast of 2.12 kg TNT, 1 ms after detonation.
6. Location of the shock-front, reaction-front, and water mist interface with (solid symbols) and without (open symbols) water mist present.
7. Maximum overpressure for a detonation of 2.12 kg TNT. 25-30 micron droplets, mass loading of 0.5.
8. Maximum overpressure for a detonation of 2.12 kg TNT. Effect of starting location of water mist on the amount of mitigation.
9. Maximum overpressure for a detonation of 2.12 kg TNT. Water amount is held constant at 9.71 kg, but mass density is varied from 0.25 to 1.0.
10. Maximum overpressure at two specific locations for different mass loadings and different droplet sizes. 2.12 kg TNT detonation. 50 cm and 150 cm from the initial explosive.
11. Temperature (top) and pressure (bottom) fields for one-quarter of the enclosure at 1, 2, 5, and 15 ms after detonation of a 2.12 kg explosive without water mist present. Temperature contour range is from 300 to 2500 K, pressure contour range is from 10^5 to 8×10^6 dynes/cm².
12. Temperature (top), pressure (middle), and water mist density (bottom) for one-quarter of the enclosure at 1, 2, 5, and 15 ms after detonation of 2.12 kg explosive with water mist present. Water mist contour range is from 0 to 0.0025 g/cm³.
13. Pressure trace at center of domain after detonation of 2.12 kg TNT without (solid) and with (dashed) water mist present. Water mist mass loading is 0.5.
14. Integrated water and water vapor mass within domain (a) and pressure development at center of the domain (b) with absorbing (solid) and perfectly reflecting (dashed) walls after detonation of 2.12 kg TNT. Water-mass loading is 0.5.
15. Blast overpressure for a 5-lb TNT charge from simulation.
16. Pressure traces for far corner location with (dashed) and without (solid) water mist present in the domain. Water mist mass loading is 0.5 for these simulations.
17. Two snapshots of the magnitude of the gradient of density for the VCE/SS test case, an axisymmetric geometry with four cylinders and a ramp. Snapshots are at 70 ms (left) and 100 ms (right).
18. Temperature solution with PARAMESH/BLAST code (FBX2), with (left) and without (right) grid. 2.273 kg TNT in a 215x215 cm domain. 16x16 base mesh size. 5 levels of refinement.

Executive Summary

This is the third in a series of reports focusing on numerical simulation of blasts and blast mitigation. The first report detailed simulation of a blast from a condensed-phase explosive, the second report detailed simulation of small (sub 50 micron) droplets and particles on shock waves. This report uses the models developed in the first two to specifically examine the effect of water mist on blast shock-fronts and the development of quasi-static pressure in enclosed spaces. Comparisons with experiments conducted at NSWC are used to validate this model.

The first set of simulations examined the multi-dimensional nature of the expanding shock-front and reaction-front after detonation of the explosive. Results showed that the reaction-front lags considerably behind the shock-front, and that the water mist is pushed outwards away from the explosive location by the shocked air gases. Therefore, the water mist does not directly suppress the secondary reactions in unconfined blasts. Quantitative simulations were conducted to determine the exact effect of water mist droplet size (from 5 to 50 microns) and mass loading on the shock-front. In these simulations, droplet size played a small secondary role compared to mass loading. Close to the explosive, the smaller droplets were actually less effective while further downstream there was an optimum droplet size depending on the mass loading. Vaporization had little effect on attenuating the shock front, which suggests that momentum extraction plays the key role in mitigation of the shock front. For these cases, the total water mass between the observer and explosive was the most important factor in determining the amount of mitigation seen by the observer.

Simulations were also conducted to determine the effectiveness of water mist to mitigate quasi-static pressure build up in enclosures and the results were compared to experimental data. The simulations were able to predict the overall mitigation efficiency of the water mist to within a few percent. Absolute values of quasi-static pressure for the simulations tended to be slightly higher than experimental values, most likely because various loss mechanisms (incomplete combustion, absorption of energy by walls and other structures, and venting) that were not incorporated into the model. Results from a simple thermodynamic model were also compared with the experimental results and tended to substantially overpredict the mitigation efficiency, suggesting that unsteady multidimensional simulations are necessary to predict mitigation efficiency. This will be particularly true when examining more complex spaces and mitigation strategies.

Finally, additional needed computational work is summarized in this report. Specifically, improved models for the explosive blast and droplet breakup, a better treatment of complex three-dimensional spaces, and grid adaption are discussed. Many of these improvements are implemented and currently being tested, and will help substantially in simulating blast mitigation scenarios of interest to the Navy and DoD.

Blast Mitigation by Water Mist

(3) Mitigation for Confined and Unconfined Blasts

1. INTRODUCTION

In spite of our best efforts at detecting and deterring unwanted explosions, current events in Iraq as well as previous incidents such as with the USS Cole and the Khobar Towers, have strikingly highlighted the need to mitigate the effects of unwanted explosions. Many of the hazards the armed services deal with overlap hazards in the commercial sector, such as propellant and explosive storage. However, the armed services also have unique requirements for reducing the effects of weapon attack, and more recently in minimizing the effects of terrorist attacks. Both of these attacks pose unique difficulties in mitigating the blast effects. Unlike storage areas for propellants and explosives or offshore oil platforms, protection from weapon attack is required for a variety of spaces that are used to perform a myriad of specialized functions. While lessons can be learnt from past experiences in the commercial sector, specific solutions will have to be tailored for DoD applications.

In the petroleum and coal industries (such as with off-shore platform or coal mine accidents), deflagrations or detonations of fuels (including coal dust) mixed with oxygen in the air is a common hazard. Mitigation of blasts in chemical processing plants, including the fireworks and propellant industries, has also received considerable attention due to the frequency and catastrophic nature of accidents. Many of these hazards have been addressed using specific methodologies for protecting these areas, such as water blankets, structural reinforcement, venting, and spacing requirements.

Unlike the specific mitigation techniques mentioned above, techniques for general military spaces have some unique requirements. Above all, they must not interfere with the function of the space while providing adequate protection from blasts. Secondly, technologies that do not require a major redesign and have the capability of being retrofitted into current platforms are also very attractive. Mitigants that not only reduce the damage from explosions but also prevent flashover to a fire are highly desirable. Lastly, the technology must also be safe for any personnel that might happen to be in the vicinity of the blast when it occurs. Water mist becomes an attractive candidate mitigant when these issues are considered.

Kailasanath *et al.* [1] reported an extensive review of the current uses of water in blast mitigation scenarios. They identified two main areas of emphasis: mitigating the effects of condensed-phase explosives by placing water in proximity to the explosive, and using water mist to mitigate vapor-cloud explosions by either inerting the mixture, quenching the flame or reducing the deflagration velocities. They also identified key issues that remained to be solved. These include determining the main mechanisms of mitigation and the effectiveness of different droplet sizes, from very small (less than 10 μm) to intermediate (20-200 μm) to relatively “large” (200+ μm) droplets. In addition, the area of water deluge or concentration of water needed for effective mitigation had to be determined. Finally, they also identified the concern that in some cases flame acceleration was observed due to turbulence, and water mist mitigation of some large

scale tests indicated that large complex systems can show less positive results than simple configurations, highlighting the need to be able to quantify the effect of water mist on mitigating explosions for large and complex structures, preferably without doing a large number of expensive experimental tests.

Some of the more recent work has extended our understanding of blast mitigation with water, while remaining focused on the two areas mentioned above. In particular, Liu *et al.* [2] modeled the mitigation of a condensed-phase explosive with water using a Lagrangian smoothed particle hydrodynamic code, looking specifically at placing a solid water shield either in contact with the explosive charge or leaving an air gap between the explosive and the water shield. They found that with an air gap, the geometry of the explosive charge and water shield shape needed to be carefully investigated to determine optimum effectiveness. For blasts in enclosures, they found the water shield was most effective in mitigating the equilibrium gas pressure rather than the peak shock pressure.

Catlin [3] studied using water containers passively for explosion suppression, examining the specific case of vented flame extinguishment. He found that an array of enclosed containers that release their water as the flame or shock wave impacts the containers can completely eliminate the external overpressure and significantly reduce the internal overpressure in a vented explosion situation. These and other passive systems have typically been the ideal solution for blast mitigation, due to the extremely fast time scales over which blasts occur. However, passive systems usually involve a redesign of the space or may otherwise interfere with the proper functioning of the space, and often require apriori knowledge of where the blast is likely to occur.

A notable study by Buzukov [4] used water curtains to reduce the overpressure of condensed-phase explosions. He showed air-water drop curtains to be highly effective at decreasing the effects of air shock waves in open explosions of a concentrated charge. They used an auxiliary charge that created an outburst of sprayed water to act as the curtain, reaching a 90% reduction in overpressures in some cases, and showed that curtains can be very effective in reducing the blast effects. Water curtains remain an attractive method for protecting many areas from blast, although the ability to generate these curtains on the scale necessary for effective mitigation may be problematic for a wide range of spaces.

One method that has been extensively researched for offshore platforms is the use of water mist or sprays for mitigation [5,6]. Water mist systems are attractive for blast mitigation for several reasons. These systems can be used in a wide range of spaces with very little redesign of the space, vaporization of water extracts energy from the resulting shock wave, and water is non-toxic to personnel and environmentally safe. In addition, these systems can serve a dual-role both as a blast mitigation and a fire protection system. Both van Wingerden [5] and Thomas [6] found that water mist can be effective at reducing deflagrations and gas explosions on large scale offshore platforms and worked through quenching and decelerating the flame. Van Wingerden found that droplets below 20 μm and above 200 μm are most effective, due to rapid vaporization of the smaller droplets and droplet breakup for the larger droplets. Both noted, however, that in certain situations water mist is not effective at mitigation of the reactions and can actually increase the flame speed and pressure buildup because of the turbulence the mist injection system generates.

With water mist systems being implemented in the machinery spaces of LPD-17 and DD(X) [7], there is considerable interest in an assessment of their capability with respect to blast mitigation. Our group has had extensive involvement in simulating the ability of water mist to suppress both gas jet flames [8,9] and liquid pool fires [10] using a multiphase simulation technique, and extension of these techniques to blast mitigation scenarios has been straight forward [11,12].

There are still several unknowns with respect to water mist systems being used for blast mitigation. First, an accurate assessment of pressure reduction due to the water mist system is essential in determining whether this system is appropriate for further investigation. In addition, the difficulty of sensing the blast in time for arming and starting a water mist system is also critical to its success as a blast mitigant, although this difficulty is experienced by all active mitigation systems, and can at least be partially circumvented in specific circumstances. An additional danger with water systems is the possibility of electrical fires when protecting areas with substantial electronics. Water mist systems may also not provide significant protection against shrapnel or projectiles from the explosion.

This report is the third in a series of reports detailing the modeling effort that has been undertaken at NRL on blast mitigation. The first report [11] discussed modeling of confined and unconfined blasts without mitigation. The second report [12] discussed in depth the modeling of the dispersed-phase, and applied this model to predict characteristics of shock waves impinging on particles or droplets. The shock waves were generated by a shock tube and presented an ideal environment to study different fundamental characteristics of particle and droplet-shock wave interaction. The present report uses the models developed in the first two reports to understand the ability of water mist to mitigate blasts both in unconfined and confined scenarios. The report draws heavily from work that was done for the 3rd Joint Meeting of the US Sections of the Combustion Institute [13] and the DDESB Explosives Safety Seminar [14], in addition to current work that was completed in support of the NRL experiments conducted at the Naval Surface Warfare Center-IHD [15].

This report is divided into six sections. The first section describes the models used for the simulations, which is included for completeness. The next section is a general overview of the properties of blasts and the interaction between the blast and water mist. The third section details the effectiveness of water mist in mitigating the front-shock from blasts. The fourth section focuses on mitigation of the quasi-static pressure in confined spaces. The fifth main section examines the characteristics of the overpressure for experiments at NSWC and draws some qualitative and quantitative comparisons between the experiment and simulations. The sixth section is a more practical application of some of the tools developed pertaining to using water mist for subway protection. In the final section, we discuss some of the new capabilities that are to meet future blast mitigation predictions.

2. NUMERICAL MODEL AND SOLUTION PROCEDURE

The approach chosen for modeling the blast and suppressant transport uses an Eulerian-Eulerian formulation, building on the large body of work that has been done here at the Lab for Computational Physics and Fluid Dynamics.

2.1 Gas-phase Model

The governing equations for the gas-phase are the inviscid, compressible form of the conservation equations for species, mass, momentum, and energy. They are written as:

$$\frac{\partial n_k}{\partial t} + \nabla \cdot n_k \mathbf{v} = \dot{w}_k + \dot{s}_{n,k} \quad (1)$$

$$\frac{\partial \rho}{\partial t} + \nabla \cdot \rho \mathbf{v} = \dot{s}_\rho \quad (2)$$

$$\frac{\partial \rho \mathbf{v}}{\partial t} + \nabla \cdot \rho \mathbf{v} \mathbf{v} = -\nabla P + \dot{s}_{mom} \quad (3)$$

$$\frac{\partial E}{\partial t} + \nabla \cdot (E + P) \mathbf{v} = \dot{s}_{erg} \quad (4)$$

where n_k is the concentration for species k , ρ is the fluid density, \mathbf{v} is the bulk velocity of the fluid, P is the pressure, E is the total energy, \dot{w}_k is the species production term from reactions, $\dot{s}_{n,k}, \dot{s}_\rho, \dot{s}_{mom}, \dot{s}_{erg}$ are the transfer source terms between the dispersed-phase and the gas-phase. Given N species, there are $N+5$ conservation equations for the gas-phase flow in three-dimensions. The relation between pressure, species concentration, and temperature is given by the modified Nobel-Able gas law:

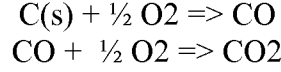
$$P = \frac{n_g R T}{1 - a n} \quad (5)$$

where n_g is the gas-phase concentration, n is the total fluid concentration, R is the universal ideal gas constant, and a is an empirical correction at high pressures to account for the effect of finite volume molecules. We use a value of $15 \text{ cm}^3/\text{mol}$ for the explosive products. The total energy is given by the relation:

$$E = \left[\sum_{k=1}^N n_k h_k(T) - \frac{P}{\rho_g} \right] + \frac{1}{2} \rho \mathbf{v} \cdot \mathbf{v} \quad (6)$$

where the species enthalpies are computed from polynomial curve-fits, and ρ_g is the gas-phase density. For the blast simulations, we track 6 species representative of the explosive products and air: solid carbon dust C(s), oxygen (O₂), water vapor (H₂O), carbon monoxide (CO), carbon dioxide (CO₂), and nitrogen (N₂). For the blast mitigation cases, we track an additional specie for the suppressant water vapor for clarity. The enthalpies for the different species are calculated using 5th-order polynomial curve-fits, given in [11].

Explosive blasts consist of a shock-front and a reaction-front located at the contact discontinuity between shocked air and explosive products. For oxygen-deficient explosives such as TNT, a secondary fireball occurs as the explosive gases are expanding and mixing with oxygen in air. For TNT blasts, this secondary fireball actually releases more energy than the explosive detonation, but is only loosely coupled with the shock-front. We model reactions occurring at the reaction-front with a two-step global model,



The reaction rates are calculated using a flame-sheet approximation, with a cut-off temperature of 700 K, below which no reactions are assumed to happen.

2.2 Dispersed-phase Model

The approach chosen for modeling the dispersed-phase is the sectional Eulerian approach introduced by Tambour [16] and expanded on by Tambour [17,18] and other researchers [19,20]. This approach has been used successfully for low speed fire mitigation studies [8-10]. The Eulerian sectional approach is appropriate for fine droplet-laden gases where the volume fraction of droplets is small but the number density is fairly large and computationally expensive for Lagrangian tracking methods. We assume a dilute mixture of spherical droplets, where the volume fraction of the dispersed-phase remains negligible (under 1%) and droplet-droplet interactions are negligible. For this paper, we consider very small droplets, in the range of 5-50 μm , and mass loadings on the order of 0.5 to 1.0. Mass loading is defined as the ratio of water mass to gas mass within a computational cell.

The dispersed-phase equations for the sectional approach are developed by grouping droplets of similar sizes together into sections. Each section is represented by Eulerian conservation equations for mass, momentum, and energy. Source terms account for mass, momentum, and energy transfer between the sections and between each section and the gas-phase. The conservation equations can be written for section j as follows:

$$\frac{\partial m^j}{\partial t} + \nabla \cdot m^j \mathbf{v}^j = -(E_1^j + E_2^j)m^j + E_1^{j+1}m^{j+1} - E_3^{j,j_{cr}}m^j + \sum_{l=j+1}^{N_s} E_3^{l,j}m^l \quad (7)$$

$$\frac{\partial m^j \mathbf{v}^j}{\partial t} + \nabla \cdot m^j \mathbf{v}^j \mathbf{v}^j = -(E_1^j + E_2^j)m^j \mathbf{v}^j + E_1^{j+1}m^{j+1} \mathbf{v}^{j+1} - E_3^{j,j_{cr}}m^j \mathbf{v}^j + \sum_{l=j+1}^{N_s} E_3^{l,j}m^l \mathbf{v}^l \quad (8)$$

$$\begin{aligned} \frac{\partial m^j h^j}{\partial t} + \nabla \cdot m^j \mathbf{v}^j h^j = & -E_1^j m^j h^j + E_1^{j+1} m^{j+1} h^{j+1} - E_2^j m^j (h^j + L_v) \\ & - E_3^{j,j_{cr}} m^j h^j + \sum_{l=j+1}^{N_s} E_3^{l,j} m^l h^l + m^j Q^j \end{aligned} \quad (9)$$

where m^j is the mass density, \mathbf{v}^j is the velocity, and h^j is the enthalpy of the water-droplets from section j , E_1^j is the mass transfer from section j to $j-1$ due to vaporization, E_2^j is the mass-transfer from section j to the gas-phase due to vaporization, $E_3^{l,j}$ is the mass transfer from section j to section l due to droplet breakup, \mathbf{F}^j is the drag force between droplets in section j and the gas-phase, and Q^j is the heat transfer between the droplets in section j and the gas-phase. The source functions for the gas-phase can be related through the following:

$$\dot{s}_\rho = \sum_{j=1}^{N_s} m^j E_2^j \quad (10)$$

$$\dot{s}_{mom} = - \sum_{j=1}^{N_s} (m^j E_2^j \mathbf{v}^j - m^j \mathbf{F}^j) \quad (11)$$

$$\dot{s}_{erg} = - \sum_{j=1}^{N_s} (m^j E_2^j (h^j + \mathbf{v}^j \cdot \mathbf{v}^j) - m^j Q^j - m^j \mathbf{F}^j \cdot \mathbf{v}^j) \quad (12)$$

The source terms E_1^j , E_2^j , \mathbf{F}^j , and Q^j are calculated based on single-droplet models and an assumption for the number density distribution in each section [20]. For each section, we assume that the number density within the section is constant with respect to droplet volume. A single droplet i is characterized by its mass $m_{d,i}$, velocity $\mathbf{v}_{d,i}$, diameter $D_{d,i}$, and specific enthalpy $h_{d,i}$. We assume the temperature is uniform throughout each droplet, therefore, there is a one-to-one correspondence between droplet temperature and specific enthalpy where the specific enthalpy can be expressed by $h_{d,i} = C_l T_{d,i}$, where C_l is the specific heat of the liquid. We assume the liquid-phase density ρ_l is constant, thus the droplet mass is simply $m_{d,i} = \rho_l (\pi D_{d,i}^3 / 6)$. For a single-droplet, the high velocity correction term is based on Clift [21], and the vaporization and heat-transfer convective corrections are based on a Ranz-Marshall correlation [22]. Calculation of the source terms is described in detail in [12]. The resulting source terms for transfer of mass from section j to section $j-1$ from droplet vaporization is

$$E_1^j = \sqrt[3]{\frac{3\pi^2}{4}} \frac{m^j \beta}{(V^{j+1})^2 - (V^j)^2} \left[(V^j)^{4/3} + A (V^j)^{3/2} \right] \quad (13)$$

where $A = 0.3(6/\pi)^{1/6} \text{Pr}^{1/3} (2\rho v_{rel}^j / \mu)^{1/2}$. The source term for transfer of mass from section j to the gas-phase from droplet vaporization is

$$E_2^j = \frac{\sqrt[3]{3\pi^2}}{4} \left[\frac{m^j \beta}{(V^{j+1})^2 - (V^j)^2} \right] \left\{ \frac{3}{4} \left[(V^{j+1})^{4/3} - (V^j)^{4/3} \right] + \frac{2}{3} A \left[(V^{j+1})^{3/2} - (V^j)^{3/2} \right] \right\} \quad (14)$$

The momentum transfer source term is computed in two parts, a non-convective and a convection correction term, described as \mathbf{F}_1 and \mathbf{F}_2

$$m^j \mathbf{F}_1^j = m^j \frac{9}{\rho_l} \sqrt[3]{\frac{3\pi^2}{4}} \left[\frac{(V^{j+1})^{4/3} - (V^j)^{4/3}}{(V^{j+1})^2 - (V^j)^2} \right] \mu (\mathbf{v} - \mathbf{v}^j) \quad (15)$$

$$m^j \mathbf{F}_2^j = m^j \frac{2.604}{\rho_l} \left[\frac{(V^{j+1})^{1.5623} - (V^j)^{1.5623}}{(V^{j+1})^2 - (V^j)^2} \right] \left(\frac{\rho v_{rel}^j}{\mu} \right)^{0.687} \mu (\mathbf{v} - \mathbf{v}^j) \quad (16)$$

Similarly, the heat transfer source term is broken into a non-convective and a convective term,

$$m^j Q_1^j = m^j \frac{3\sqrt[3]{6\pi^2}}{C_l \rho_l} \left[\frac{(V^{j+1})^{4/3} - (V^j)^{4/3}}{(V^{j+1})^2 - (V^j)^2} \right] \lambda(T - T^j) \quad (17)$$

$$m^j Q_2^j = m^j \frac{2.654}{\rho_l} C_l \text{Pr}^{1/3} \left(\frac{\rho v_{rel}^j}{\mu} \right)^{0.55} \left[\frac{(V^{j+1})^{1.5167} - (V^j)^{1.5167}}{(V^{j+1})^2 - (V^j)^2} \right] \lambda(T - T^j) \quad (18)$$

In addition to drag, heat transfer, and vaporization, droplet breakup must also be accounted for when large droplets ($>100 \mu\text{m}$) are considered. The current research has focused on small droplets where breakup is not important and is neglected.

2.3 Property Evaluation for Blast Mitigation Models

For the dispersed-phase, we need to calculate as a function of temperature the saturation pressure of water, the viscosity and conductivity of the gas mixture, and the surface tension of the water. Note that all of the properties are given in CGS units. The saturation pressure for water vapor with respect to temperature is curve-fit using Antoine equation with widely available data:

$$P_{H_2O,sat}(T) = 1.20967 \times 10^5 \exp\left(-\frac{3835.83}{T - 45}\right) \text{ dynes/cm}^2 \quad (19)$$

where the pressure is in bars and the temperature is in Kelvins. These coefficients produce an error of less than 2% over most of the data compiled in *Steam Tables* [23]. Near the supercritical temperature (above 600 K) this error increases slightly to under 5%.

The Sutherland expression is used for expressing viscosity as a function of temperature:

$$\mu(T) = 1.458 \times 10^{-7} \left(\frac{T^{3/2}}{110 + T} \right) \text{ dynes}\cdot\text{sec/cm}^2 \quad (20)$$

for a mixture containing predominantly air. The thermal conductivity is calculated assuming a constant Prandtl number of 0.75, and the surface-tension is calculated using a linear relation with temperature, assuming that the surface tension at the critical temperature for water vanishes,

$$\sigma(T) = 72.8 - 0.219(T - 293) \text{ dynes/cm}. \quad (21)$$

$C_l = 4189.4 \times 10^4 \text{ erg/gm K}$, and the liquid density of water is assumed constant at 1 gm/cm^3 for the simulations. The latent heat of vaporization is calculated

$$L_v = 2304.9 \times 10^7 + [h_{H_2O}(T) - \Delta \mathcal{H}_{f,H_2O}^o] - C_l(T - 298) \text{ ergs/gm}. \quad (22)$$

2.4 Solution Procedure

The solution procedure involves solving $M+1$ sets of conservation equations, where M is the number of sections being simulated. Each set contains a continuity equation, momentum equation, and an energy equation and is coupled through source terms. The present procedure used for solving these conservation equations is by a time-step splitting method. Each set of conservation equations is solved independently using the explicit

FCT-algorithm of Boris and Book [24], and is described in detail in [25]. The cross-coupling source terms are added explicitly at the end of the dispersed-phase step. Parallelism is accomplished through domain decomposition using the Multiblock PARTI library [26].

Initial conditions for the explosions are obtained by doing a constant-volume reaction calculation for the explosive within its volume. This gives an initial pressure, temperature, and species concentrations for the volume, which then expands outwards when the simulation begins. The solution procedure and initial condition are explained in more detail in [11]. Our simulations have all focused on TNT explosions; however, other explosives could easily be substituted using this initialization procedure. Data for other explosives is provided in Appendix A. Verification and validation of the solution procedure for blasts and particle interactions has been reported in [11,12].

2.5 Wall Boundary Conditions for the Water mist

Wall boundary conditions present a problem for dispersed-phase flows using the Eulerian approach because of the difficulty of accurately representing the droplet momentum distribution near a wall where droplets are being partially reflected. In an Eulerian representation, any characteristic of a given droplet (such as momentum or temperature) is represented by the average of all of the droplets within that cell. This representation becomes a problem when you have two streams of droplets heading towards each other as shown in Figure 1. For relatively dispersed droplets, these two populations of droplets physically tend to go straight through one another. However, with the Eulerian approach, the momentum at each cell is taken as the average momentum of all of the droplets within that section. Thus, the end result is one large mass of water droplets heading at a velocity dependent on the averaged momentum, as shown in Figure 1b. With reflecting walls we have a similar situation. As the water droplets hit the wall, the reflected water droplets have a velocity directly opposite of the initial (non-reflected water droplets). This is shown in Figure 2.

With the sectional approach, droplets are broken into groups dependent on the size of the droplets. This still presents problems for modeling reflection off of the wall, because the only property that differentiates the groups is droplet size. One approach to more accurately simulate the boundary condition is to create another group of sections that represent only reflected drops. Interaction between the reflected drops and the non-reflected drops occurs only through the boundary condition, and in all other ways, the reflected droplet sections behave like the non-reflected droplets. Since the reflected sections need to be transported similarly to the non-reflected sections, this method does effectively double the cost of the dispersed-phase calculation; however, it is possible to make some assumptions to optimize the solution. In terms of the conservation equations, we now have sections j and j_r , where j_r represents the new reflected section, with mass, momentum, and energy conservation equations representing all of the sections.

The boundary condition can now be written in a very general manner. The wall flow is treated as an outflow boundary for the non-reflected sections. The mass, momentum, and energy flux for section j out of the wall is dependent on the perpendicular boundary cell velocity, v_{\perp}^j , where $v_{\perp}^j < 0$ means the mass flux is away from the wall, and $v_{\perp}^j > 0$ means that the mass flux is towards the wall. If v_{\perp}^j is less than zero, we treat the wall as a wall and set the interface velocity v_{int}^j to 0. If, on the other hand, v_{\perp}^j

is greater than zero, we treat the wall as an outflow boundary with $v_{\text{int}}^j = v_{\perp}^j$. For the reflected sections, the wall interface is treated as a inflow boundary condition. This boundary condition is dependent on the outflux for the non-reflected sections and on reflection coefficients, α^{j,j_r} . The reflection coefficients are between 0 and 1, and represent the transfer of mass, momentum, and energy from section j to section j_r . The inflow mass, momentum, and energy fluxes are written as:

$$\begin{aligned}
m_{\text{fluxin}}^{j_r} &= \sum_{j=1}^M \alpha^{j,j_r} m_{\text{fluxout}}^j \\
(m^{j_r} \mathbf{v}^{j_r})_{\text{fluxin}} &= \sum_{j=1}^M \alpha^{j,j_r} (m^j \mathbf{v}^j)_{\text{fluxout}} \\
(m^{j_r} h^{j_r})_{\text{fluxin}} &= \sum_{j=1}^M \alpha^{j,j_r} (m^j h^j)_{\text{fluxout}}
\end{aligned} \tag{23}$$

For the simulations presented in this report, we focus on two cases. The first considers a wall with a reflection coefficient of 1, the second case considers a wall with a reflection coefficient of 0, where the droplets reflect elastically off of the wall. To simplify the representation, we make the further assumption that droplets of a given size that reflect off of the wall will remain that size. That is, $\alpha^{j,j_r} = 1$ if and only if $j=j_r$, otherwise $\alpha^{j,j_r} = 0$.

For very complicated flows, this method may become problematic. For instance, what if reflected droplet sections j_r reverse direction and impinge on the wall again. Currently this situation is ignored, and it is assumed that they will remain within the computational domain. This should work for blast mitigation simulations, because the main reflection that we are interested in capturing is the initial reflection due to the shock-front. There is no clear way to do anything above this with the Eulerian sectional approach without a much more significant cost.

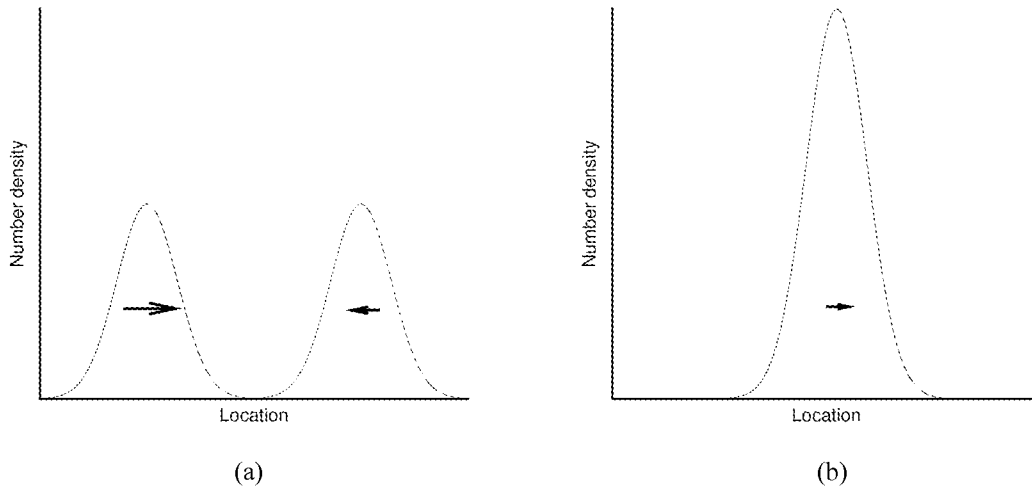


Figure 1. Example of Eulerian treatment of two independent streams. As the streams in (a) come together, they will merge into one large stream with one momentum (b). For very dispersed streams, this is not physically accurate because the streams will tend to pass through each other.

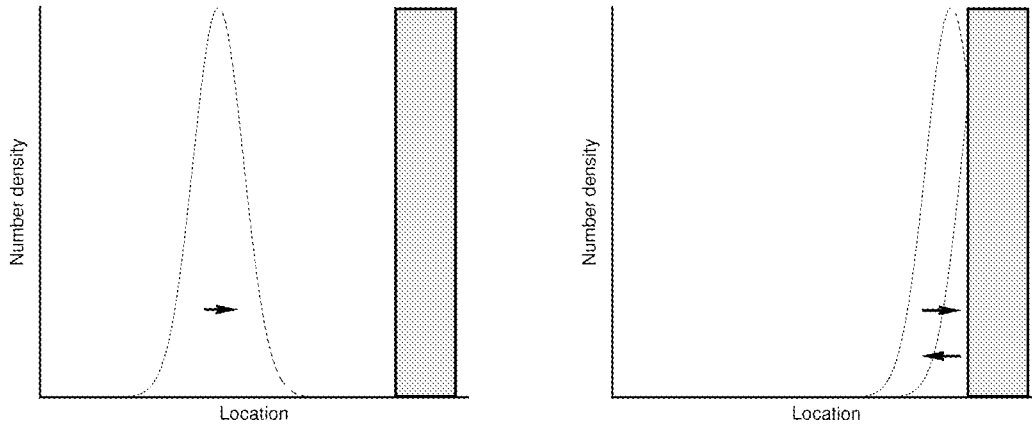


Figure 2. Number density as a stream of droplets hit a wall. As it is hitting the wall, droplets will be reflected and reverse in direction. This is difficult for an Eulerian treatment of droplets to reproduce accurately.

3. BLAST MITIGATION USING WATER MIST

As discussed extensively in [11], an explosive blast consists of two important regions: the front-shock, which is essentially an air shock, and a reaction-front, where the shocked air gases mix with the excess explosive fuel and burn. Mitigation is dependent on the interaction of the water mist both with the shock-front and the reaction-front. To understand these concepts better, we show an axisymmetric solution for the temperature

and pressure for a detonation of 2.12 kg TNT, 1 ms after detonation of the explosive. The charge size and dimensions were selected because of their similarity to previous experiments using water to mitigate blasts [27]. The cell size for the computations is roughly 0.33 cm x 0.33 cm, and the domain extends out for 200 cm. This particular case has no water mist present in the domain.

Both these regions are shown in Figure 3 on a temperature and pressure distribution plots at one instant of the multi-dimensional simulation. As seen in the figure, the reaction-front is far behind the shock-front and does not contribute to the shock-front overpressure. This is generally true except for immediately after the detonation when the shock-front is still close to the location of the explosive. The reaction-front does become important, however, for the development of overpressure in enclosures. For that reason, we simulate both the explosive product gases and oxygen in the air, allowing us to track the reaction-front and the heat release due to secondary reactions. For multi-dimensional simulations, the reaction-front is physically unstable and becomes wrinkled, most likely due to some form of Rayleigh-Taylor instability.

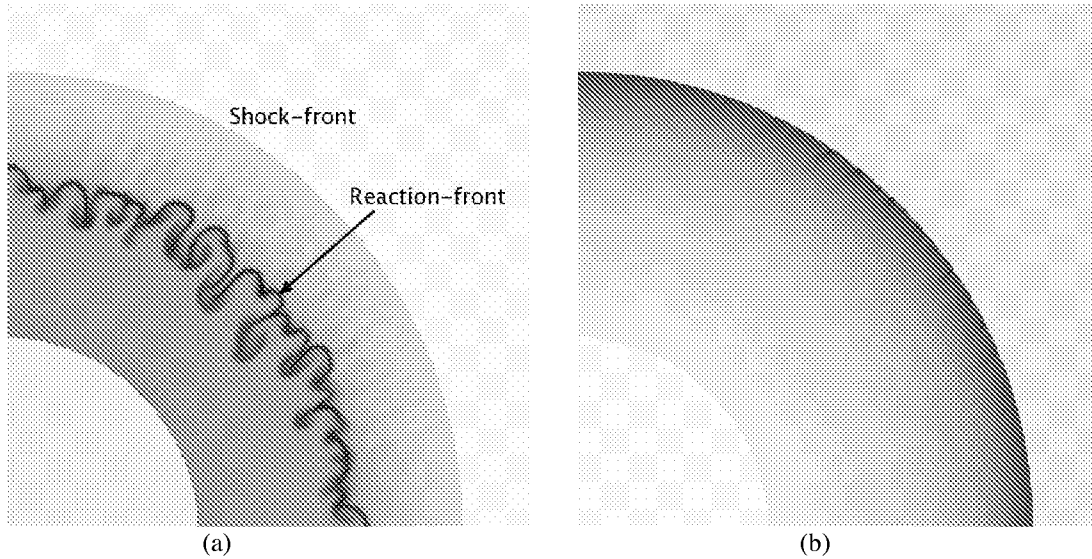
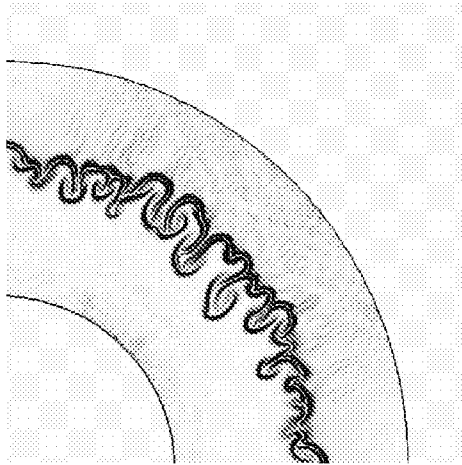
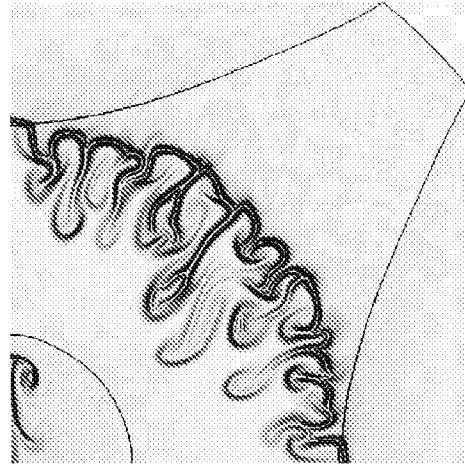


Figure 3. Temperature (a) and pressure (b) for axisymmetric explosion of 2.12 kg TNT, 1 ms after detonation. Maximum temperature is 2100 K, maximum pressure is 9.1 bar.

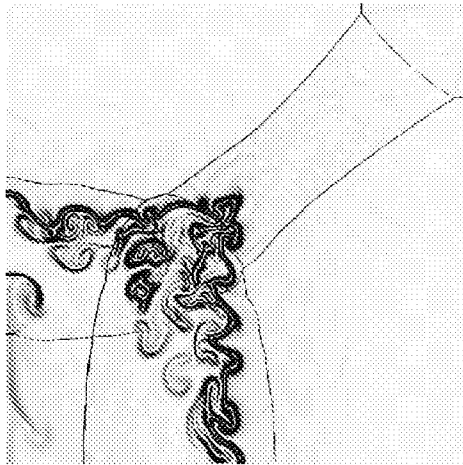
The situation becomes more complex in enclosures. Initially the same shock-front and reaction-fronts are present immediately following the detonation. As the shock-front is reflected off of the wall, the flow field quickly becomes very complex with reflections happening in several different directions. We demonstrate this by showing a series of temperature gradient plots for the same representative case in Figure 4. The temperature gradient shows the shock-front and reflected shock waves as sharp lines, while the reaction-front is a more diffuse wrinkled line. As shown in the figure, there is considerable interaction between the reaction-front and the reflected shock waves, which tends to increase the mixing and drive the reactions towards completion. In an enclosure, the release of energy from the reactions results in an increase in the average temperature and thus the quasi-static pressure within the domain.



(a) 1.0 ms



(b) 2.0 ms



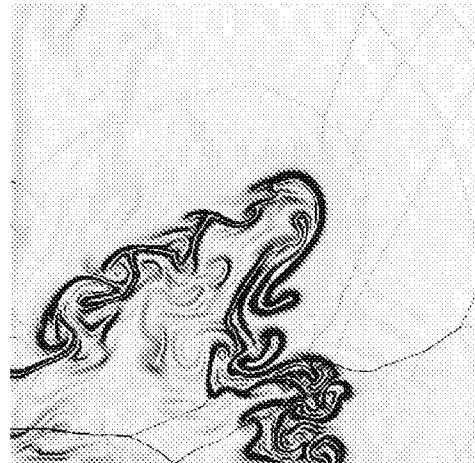
(c) 3.0 ms



(d) 4.0 ms



(e) 5.0 ms



(f) 6.0 ms

Figure 4. Magnitude of the gradient of the temperature for an axisymmetric explosion of 2.12 kg TNT. Temperature gradient is saturated at 250 K/cm. Domain length and radius is 200 cm.

The addition of water mist into the domain complicates the situation. For the example problem, water mist is evenly dispersed throughout the domain at a mass loading of 0.5. Similar to the air, water droplets are initially pushed away from the source of the explosion as the blast wave expands, but behave differently due to their inertia. We can draw a surface separating where water mist is present and not present, called the water mist interface. In order to quench any of the secondary reactions, this surface must penetrate into the explosive gases. For multi-dimensional simulations, we approximate this surface by computing the gradient of the water mist density field. Similarly, by computing the gradients of the pressure field and the CO concentration field, we determine the locations for the reaction-front and shock-front. These three plots are superimposed to determine the relative positions of the shock-front, reaction-front, and water mist interface for a representative solution in Figure 5. The water mist interface is clearly outside of the reaction-front and therefore does not play a strong role in suppressing the secondary reactions.

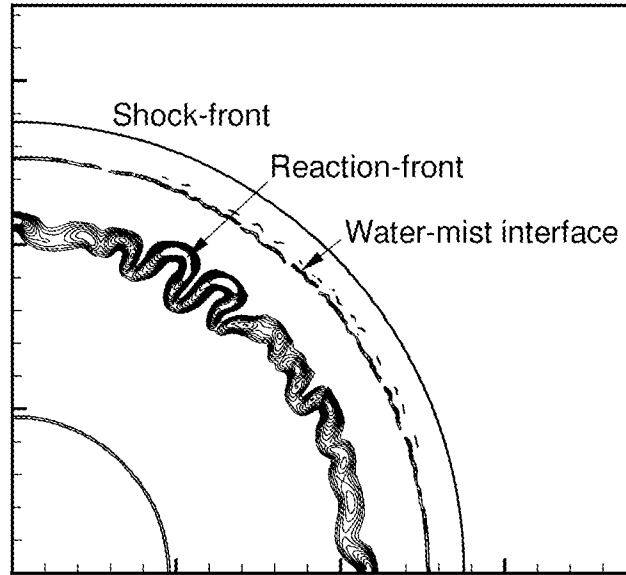


Figure 5. Gradient of pressure, water mist, and CO concentration for a blast of 2.12 kg TNT, 1 ms after detonation.

Using spherically-symmetric simulations, we calculate the location of this interface along with the reaction-front and shock-front on an $x-t$ diagram, as is shown in Fig. 6. Although the water mist penetrates into the explosive products initially, the inertia of the droplets tend to push the water mist out of the reaction zone as the gases contract after the over-expansion. The results above suggest that spherically-symmetric solutions are adequate to understand the mitigation of the front-shock using water mist in unconfined spaces.

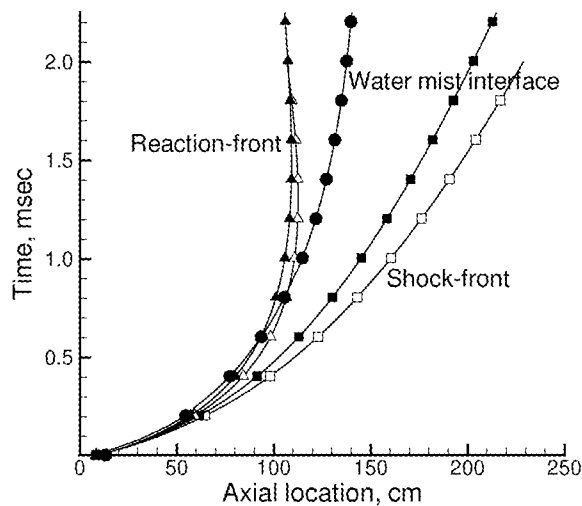


Figure 6. Location of the shock-front, reaction-front, and water mist interface with (solid symbols) and without (open symbols) water mist present.

4. MITIGATION OF THE SHOCK-FRONT

This section focuses on a series of results that examine in more detail the effect that water mist has on the shock-front. For these simulations, we use spherically-symmetric simulations. We increase the resolution to 0.173 cm per cell and increase the distance that we examine to 250 cm. The charge consists of 2.12 kg (4.67 lb) of TNT. The time-steps taken in the simulation vary depending on the strength and velocity of the shock, the presence of water mist, and the size of the water mist droplets, but are typically in the range of 1×10^{-8} s to 2×10^{-7} s. For the mitigation cases, the water mist is divided into 6 sections, with maximum droplet sizes ranging from 15 μm to 50 μm . The simulations assume a mono-dispersed droplet distribution, that is, all of the water mist mass is initially placed within the largest section. This is done (as opposed to using a more practical droplet distribution) to obtain better clarity in interpreting these results.

One of the attractive features of water for mitigation and suppression of explosions and fires is the large latent heat of vaporization and heat capacities of water. From numerous results on fire-suppression using water mist, this feature plays a critical role in being able to extract energy to cool the fire and suppress reactions. One may desire to naturally extend this observation from the realm of fire suppression to blast mitigation. Our first interest is to determine exactly how critical of a role vaporization plays in mitigating the shock-front. Therefore, using simulations, we simply turn off vaporization to examine the difference between a mitigated shock-front with vaporization and without vaporization. The result is summarized in Figure 7, which shows the maximum overpressure at different distances from the explosive. Interestingly, there is very little effect due to vaporization, particularly close to the explosive, where more vaporization should be taking place. This effect is due to two causes. First, the amount of water that is vaporized directly in the shock wave is fairly small, because the temperature is not extreme and the time is very short. Second, the water that is vaporized

contributes to the gas-density at the shock-front, and thus also adds into the gas pressure, partially canceling out the effect of lowering the pressure through lower gas temperatures. This suggests that most of the mitigation for the shock-front using water mist is through momentum extraction.

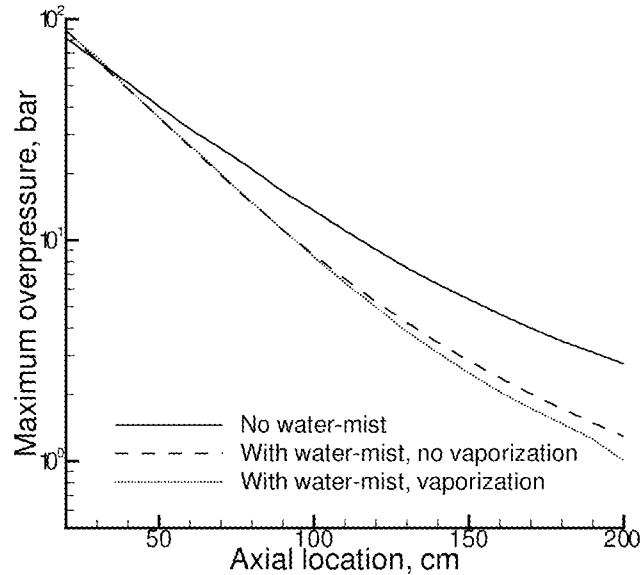


Figure 7. Maximum overpressure for a detonation of 2.12 kg TNT. 25-30 micron droplets, mass loading of 0.5.

After simulations focusing on the mechanisms involved, we undertook parametric studies. Only the highlights from a few key cases are presented here. All of the cases discussed here are done assuming vaporizing droplets from 25-30 μm , unless otherwise specified, and a mass loading of 0.5. In particular, we are interested in the effect of water mist location for effective mitigation. Unlike many blast protection scenarios, when protecting against a terrorist or weapons attack, the location of the explosion is not necessarily known beforehand. Therefore it is prudent to understand the effect of water mist location relative to the blast.

The first set of cases to investigate the effects of water mist location is shown in Figure 8. This shows the overpressure decay for mitigated and unmitigated cases, where the beginning of the water mist spray is located at different distances from the initial explosion. Three different distances are shown in this figure: 15, 25, and 50 cm. Distances of 15 or 25 cm make very little difference on the eventual mitigation. Water mist spray starting 50 cm away from the blast has a more pronounced effect, but it is still relatively small (and becomes smaller with distance.) The important conclusion from this plot is that it appears to not be necessary to have the water mist right up against the explosive, so long as it is relatively close.

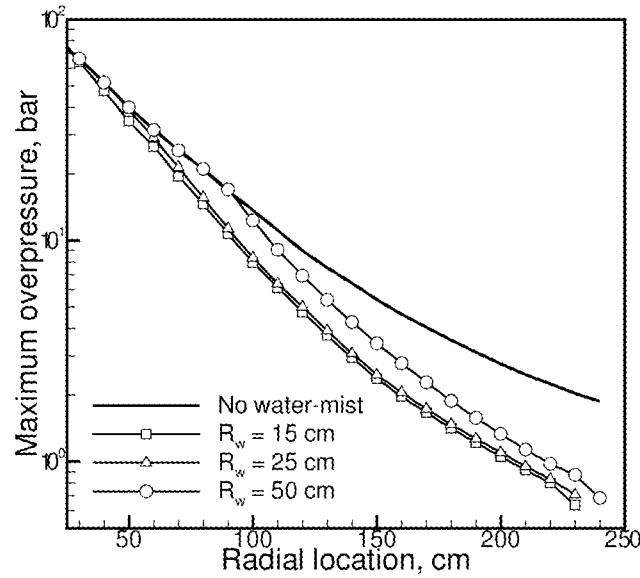


Figure 8. Maximum overpressure for a detonation of 2.12 kg TNT. Effect of starting location of water mist on the amount of mitigation.

The next parametric study of interest involves keeping the total amount of water constant, but varying the density of the spray around the explosive from a mass loading of 0.25 to 1.0. In all cases the total amount of water is 9.71 kg. From the results shown in Figure 9 we see that although the decay curves are different for each case, after the shock wave has passed through the water, the subsequent decay curve between the three cases is very similar. There is, in fact, only a very small difference in the overpressure felt by an observer at 2.4 m regardless of which mass loading was used, which suggests that a fairly diffuse spray can be as effective as a concentrated spray around the explosive. This is a promising result for using water mist for blast mitigation, because it suggests water mist can be as effective as having a more dense “water wall” surrounding the explosive provided that the total mass of water is similar.

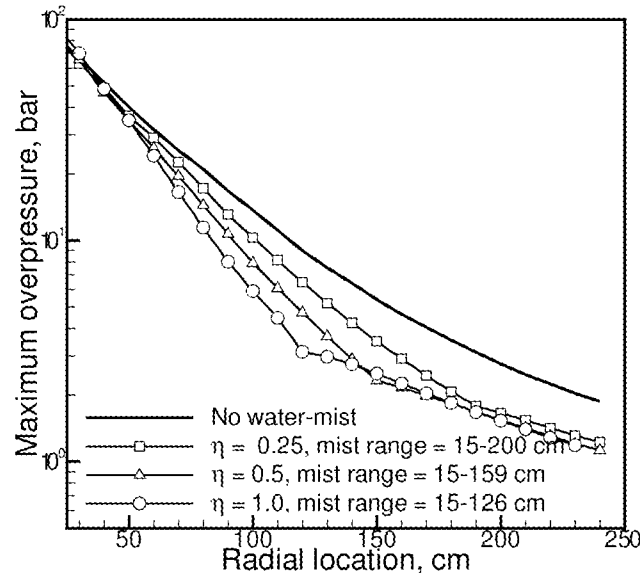


Figure 9. Maximum overpressure for a detonation of 2.12 kg TNT. Water amount is held constant at 9.71 kg, but mist density is varied from 0.25 to 1.0.

Another parametric study looked at the effect of both mass loading and droplet size, examining droplets from 7.5 μm to 50 μm , and mass loadings from 0.25 to 2.0. For all of these cases the water mist starts 15 cm from the center of the explosion and continues throughout the domain. For these simulations, we look at the overpressure at two specific locations downstream of the initial explosion, one close to the initial explosion (50 cm), and another location further away (150 cm). The results are shown in Figure 10. Again, the results mirror what we saw earlier, where closer to the explosive the mitigation is much smaller (and in some cases, we actually see an increase in overpressure) and further away we see much better mitigation. Physically, the amount of mitigation that is seen is closely related to where the maximum overpressure is developed with respect to the original explosive location. Several parameters effect this location, but the most important are mass loading and droplet size through a relaxation and transition region. It is the complex interplay of these three effects (mass loading, relaxation zone, and transition region) that determines what the optimal droplet size is at a given distance from the original explosive. Droplet size appears to play a small secondary role when compared to the mass loading, especially far away from the initial explosive. An interesting aspect of these results is that they suggest close to the water the smaller droplets are actually less effective at mitigation (although nothing mitigates effectively), and further down there seems to be an optimum droplet size dependent on the mass loading.

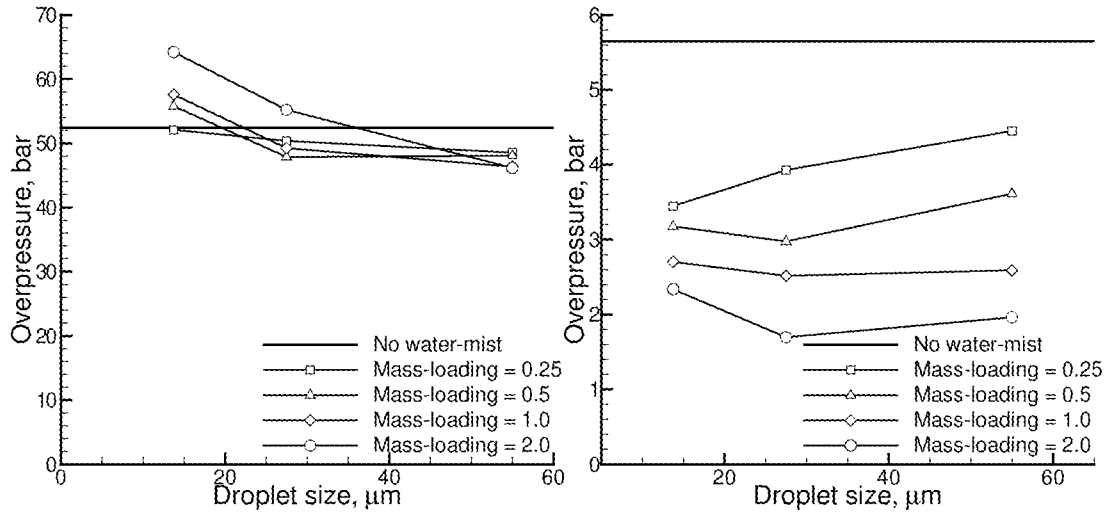


Figure 10. Maximum overpressure at two specific locations for different mass loadings and different droplet sizes. 2.12 kg TNT detonation. 50 cm and 150 cm from the initial explosive.

5. MITIGATION OF QUASI-STATIC PRESSURE

In addition to the peak overpressure, structures are also vulnerable to the impulse generated over time after the shock-front impacts the object. Impulse is defined as the integral of overpressure over a time interval:

$$I(t_1, t_2) = \int_{t_1}^{t_2} P(\tau) d\tau \quad (24)$$

where the explosive detonates at time $t=0$. For unconfined explosions, the impulse is closely tied to the shock-front pressure, and occurs over a time period that is on the order of microseconds. For confined explosions, the impulse related to the shock-front is small compared to the impulse related to longer-term pressure buildup within the enclosure, often called the quasi-static pressure. Quasi-static pressure is caused by both the initial blast and also the afterburn of excess fuel from the explosive. The pressure buildup generally occurs on the order of 0.01 to 0.1 seconds (although this varies with the size of the explosive and enclosure). For a completely sealed enclosure, the quasi-static pressure will remain constant indefinitely after the initial buildup. The quasi-static pressure is an average pressure that is defined by the impulse:

$$P_{qs}(t_1, t_2) = \frac{I(t_1, t_2)}{t_2 - t_1} \quad (25)$$

where the time intervals are typically on the order of 0.1 seconds. Unlike the blast overpressure, quasi-static pressure is not strongly dependent on location from the explosive. The buildup time interval is very long compared to the shock-front pressure pulse, but very quick relative to human reaction. Mitigation of the quasi-static pressure rise can be accomplished through two separate mechanisms. First, the pressure can be reduced simply by removing energy from the gases via vaporization. Second, if the water penetrates the reaction front, it may lower the temperature enough within the reaction front to quench the reactions.

To better understand mitigation of the quasi-static pressure, we ran two-dimensional simulations that examined specifically the buildup of quasi-static pressure and mitigation of this pressure. For these simulations, we again used 2.12 kg of TNT and enclosed it in a cylindrical container that was 3.46 m long and had a radius of 1.73 m. This corresponds to a volume of 32.5 m³, which is very close to the volume used in the NCEL experiments [27]. For the gas-boundary conditions on the outer walls, we use simple reflecting, no heat-loss boundary conditions. Unlike the previous simulations, these simulations are run for relatively long periods (50-60 ms), and the reflection of blast waves off of the walls are an important aspect of the solution. For this reason, they are also very numerically intensive, as they require good resolution of the shock wave interactions, in addition to having a long simulation time. As shown in [11], the wrinkling is essential for appropriate mixing of the excess fuel and oxygen in the air, therefore multi-dimensional simulations are required for quasi-static pressure calculations.

The first set of results we show for quasi-static pressure rise are the temperature and pressure fields without water mist present in the enclosure. These are shown in Figure 11 at 1, 2, 5, and 15 ms after detonation of the explosive. At 1 ms, before the shock wave hits the outer wall, one can see the location of the shock-front, the reaction-front where the explosive products are mixing with the shocked air gases. At this point, the reaction zone temperature is approximately 1800 K, the shocked air temperature is approximately 700 K, and the explosive products temperature is about 1300 K. The explosive gases are still expanding slightly at 2 ms (one can also see the further development of instabilities within the reaction zone), but the reaction zone is then forced back towards the interior from the reflected shock wave at 5 ms. The reflected shock increases the mixing and at this point the reaction zone temperatures increase

significantly, generally rising to around 2200 K with some spots significantly hotter. Secondary reactions continue as the reaction zone drifts towards the outer walls, with the maximum temperature now at 2500 K in several regions. The pressure starts out with very distinct shock waves and high and low pressure regions, but by 15 ms it is clear that the overall pressure in the enclosure has risen considerably and is more homogeneous.

The second set of solutions we show are the temperature, pressure, and water mist density fields when water mist is present in the enclosure, as shown in Figure 12 at 1, 2, 5, and 15 ms. These solutions are both qualitatively and quantitatively very different from the preceding solutions (without water mist) shown in Figure 11. For these solutions, the water mist has penetrated through the shocked air gases and has affected the reaction-front. At 1 ms, temperatures in the shocked air gases vary from 580 K near the shock front to 430 K near the reaction front. Because the water mist has penetrated into the reaction zone, the temperature in that region has been reduced to between 700 to 900 K. According to our simple extinguishment criteria, the secondary reactions are still occurring. At 5 and 15 ms the temperature profiles follow the basic pattern seen in Figure 11; however, the water mist has reduced the temperature quite significantly, and the amount of mixing also appears to be less. As water continues to vaporize, we expect the temperatures to continue to go down within the enclosure. The pressure behaves qualitatively similar to that observed in Figure 11, although at 15 ms we see that the overall pressure is less than in the case without water mist. Figure 13 shows a sample pressure trace at the center of the domain, and shows that the pressure rise is reduced using water mist. For longer times, the pressure within the chamber is reduced further until it attains a quasi-static value.

Examining the water mist density in Figure 12, we clearly see the water mist being pushed towards the outer wall, and for the most part staying near the outer edge of the domain. Because of the reflected shock wave, much of the water mist is slowed and vaporized before reaching the wall, thus only a small amount of water mist is actually lost to the walls in these simulations. An implication of the location of the reaction zone and the water mist is that the water mist will not directly suppress the secondary reactions. This is due to the water mist being pre-dispersed into the enclosure. In a more practical scenario, the system would be designed to continue to pump water into the area affected by the explosion and would most likely be more capable of penetrating into and suppressing the secondary reactions.

The second set of results are a comparison of the reflecting and absorbing wall boundary conditions. Figure 14 shows the total mass of liquid and vapor water integrated over the entire domain. For the reflected case, we expect the total amount of water (liquid and vapor) to remain constant. In the plot, there is a slight increase in this number, due to numerical error with the spreading of the water, and then this value stays constant as expected. With the absorbing walls, we see a distinct dip in the total amount of water (liquid and vapor) at 100 microseconds, due to the first wave hitting the wall. Surprisingly, no more water is absorbed by the wall. This is because the reflected shock wave hits the droplets and either vaporizes or deflects them away from the wall before they hit. The amount of water hitting the wall should be strongly dependent on droplet size, however, this has not been investigated.

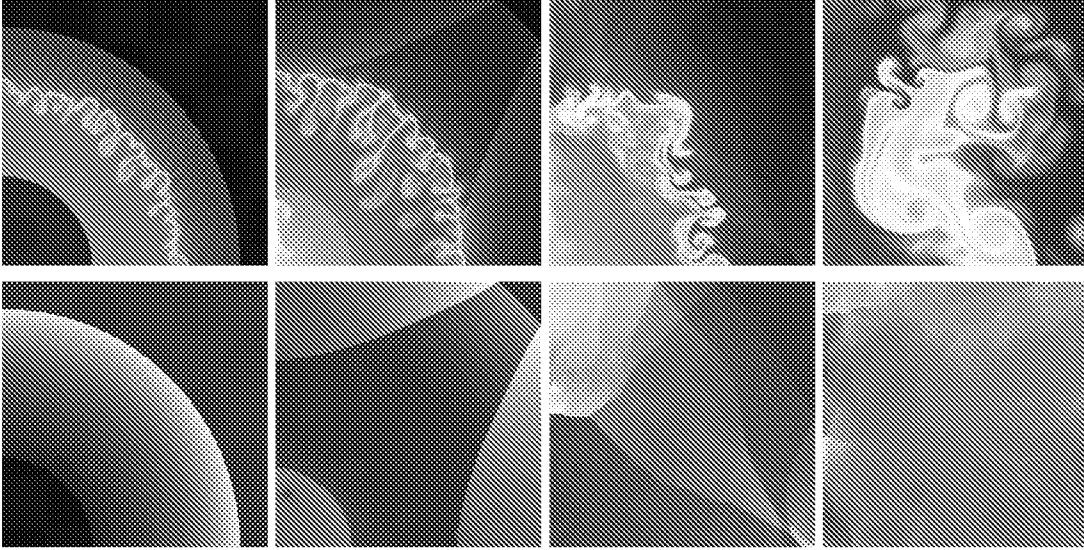


Figure 11. Temperature (top) and pressure (bottom) fields for one-quarter of the enclosure at 1, 2, 5, and 15 ms after detonation of a 2.12 kg explosive without water mist present. Temperature contour range is from 300 to 2500 K, pressure contour range is from 10^5 to 8×10^6 dynes/cm².

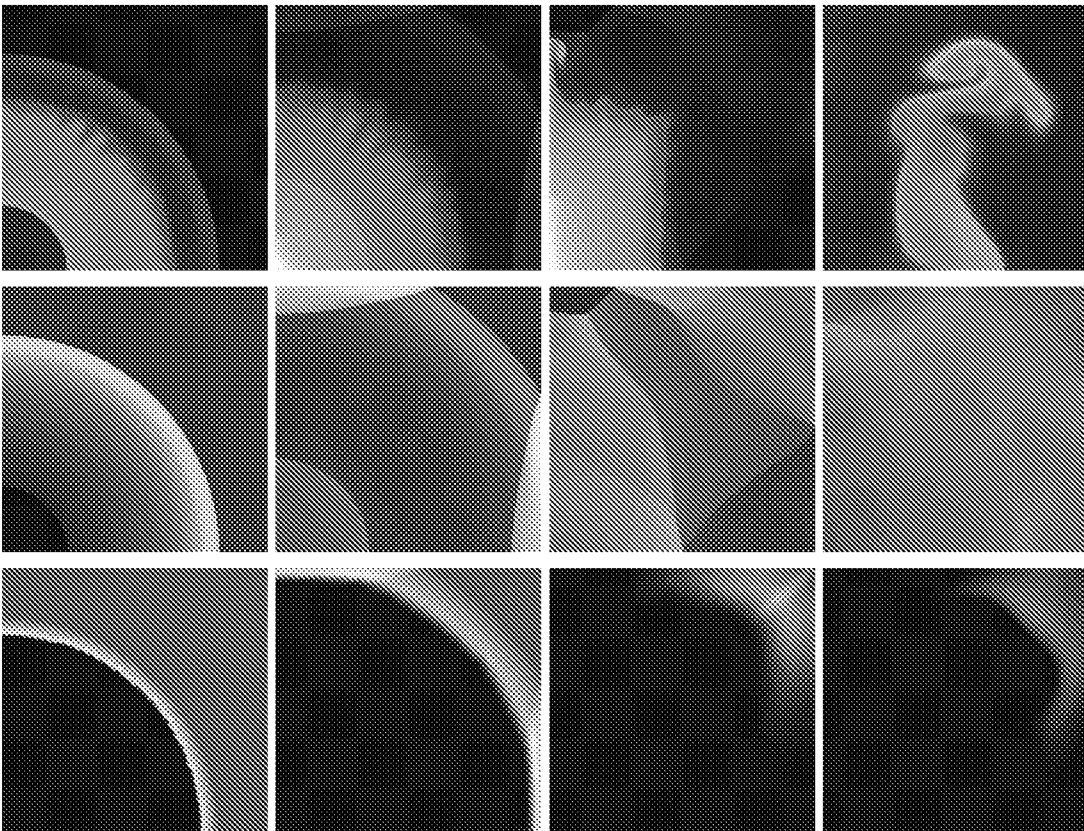


Figure 12. Temperature (top), pressure (middle), and water mist density (bottom) for one-quarter of the enclosure at 1, 2, 5, and 15 ms after detonation of 2.12 kg explosive with water mist present. Water mist contour range is from 0 to 0.0025 g/cm³.

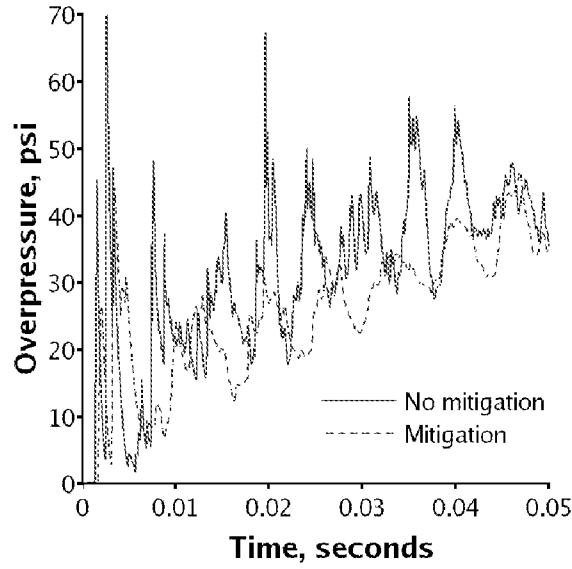


Figure 13. Pressure trace at center of domain after detonation of 2.12 kg TNT without (solid) and with (dashed) water mist present. Water mist mass loading is 0.5.

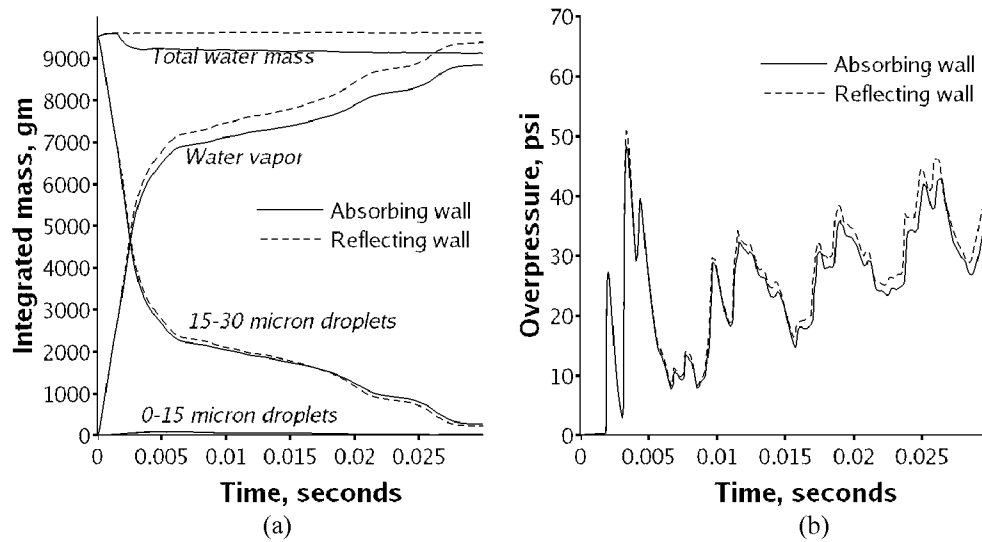


Figure 14. Integrated water and water vapor mass within domain (a) and pressure development at center of the domain (b) with absorbing (solid) and perfectly reflecting (dashed) walls after detonation of 2.12 kg TNT. Water-mass loading is 0.5.

6. COMPUTATIONS IN SUPPORT OF INDIAN HEAD EXPERIMENTS

In addition to the previous studies, we have also completed a number of simulations to support the experiments of Bailey *et al.* [15]. In the experiments, the explosive charges consisted of a large cylindrical TNT charge with a small pentolite charge and a metal blasting cap placed on the TNT charge. The pentolite functioned as an accelerator and was about 50 gms, whereas the TNT varied between 800 gms (2 lbs) to 3180 gms (7 lbs). The charge was hung from a metal chain in the center of the chamber using duct tape, with the axis of the explosive charge vertical. The blast chamber was approximately 15x15x10 ft (15x15 ft plan). Four pressure transducers were located at each of the corners, approximately halfway up the wall. The transducers were protected by a metal box approximately 1/2 ft by 1/2 ft, such that only the sensor tip was subjected to the extreme pressures and explosive products. The approximate distance from the explosive to the transducer is about 10.5 ft.

Due to the limited time and resources available to address this problem, no attempt was made to try to reproduce the details of the specific experiments. Two types of analysis are discussed below: a first order thermodynamic analysis and a more detailed two-dimensional axisymmetric numerical simulations. Because of the inherent differences between the experimental set-up and the simplified analysis and simulations, quantitative differences in the absolute values of the local parameters are to be expected. These can be minimized by looking at trends and relative differences between unmitigated to mitigated parameters. Furthermore, it must be remembered that it is extremely difficult to make highly resolved measurements and computations of these hostile and complex environments.

The water mist system in the experiments was based on the Marioff Hi-Fog system [28]. Six nozzles were placed around three walls of the blast chamber (no nozzles were on the front-wall with the door), about half-way up the walls. Discharge of all of the water (approximately 50 liters) took around 40 seconds. For the 2-lb and 5-lb blast cases, the explosive was detonated after the water mist system had been activated for 30-seconds. For more details on the water mist system setup and discharge, consult [15]. In the experiment, a substantial portion of the discharged water will collect on the walls and accumulate on the floor, although an accurate assessment of this is difficult to obtain. There is also no published measurements of the total amount of water discharged at the time of the explosive detonation. For these calculations, we assume that the amount of water discharged at the detonation time is only about 37 liters (not the full 50 liters available), resulting in a mass loading of 0.5.

To get some idea of the type of overpressures to expect, we conducted an analysis using empirical correlations and thermodynamics. First we determined the scaled mass of the explosive and the scaled distance to the pressure transducers. From there, we consulted correlations from Kinney and Graham [29] to determine the front-shock overpressure and arrival time. The quasi-static pressure and mitigated quasi-static pressure are obtained from a thermodynamic analysis outlined in [30].

Table 1. Predicted front shock overpressure and quasi-static overpressure.
Scaled weight assumes temperature of 298 K and pressure of 1.013 bar for tests.

Case	Scaled Weight	Scaled Distance	Shock Front Overpressure (psi)	Shock Front Arrival (ms)	Quasi-Static Overpressure (psi)	Mitigated Quasi-Static Overpressure	Mitigation Effectiveness
2-lb	6.44	0.502	~9.9	~4.5 ms	12.19	2.48	79.7%
5-lb	8.74	0.370	~20.3	~3 ms	28.79	6.48	77.5%

In the experiments, four pressure transducers at the corners of the chamber obtained high speed pressure data. The data was taken at 10 μ s intervals for between 1.5 to 2.5 seconds after the detonation. The blast chamber vents explosive products after the detonation. The highest average pressure occurs within 0.1 seconds after the blast; after which this overpressure begins to drop. For quasi-static pressure measurements, the data was averaged in 0.1 and 0.05 second intervals after the arrival of the first shock at the pressure transducers. There is very little difference between the 0.05 second average and the 0.1 second average during the first 0.1 seconds, we have chosen to use the 0.05 second averages in this report. Details and results from the experiment are given in [15].

The current numerical procedure can compute either three-dimensional or two-dimensional axisymmetric simulations. For three-dimensional geometries, quasi-static pressure calculations tend to be very challenging due to the resolution requirements for resolving the shock waves and the long time scales required for quasi-static calculations. We have therefore chosen to do two-dimensional axisymmetric simulations for the quasi-static pressure calculations. This means that some of the quantitative characteristics are different than seen in the experiments, however, the qualitative characteristics should be similar, and the quasi-static pressure changes should be comparable. To ensure consistency between the experiment and simulations, we have chosen a cylindrical domain with the same volume as the experimental blast chamber, 2250 ft³ or 63.7 m³. We have selected a cylinder with nearly a 1:1 ratio, radius of 215 cm and a half length of 219 cm. By doing two-dimensional axisymmetric simulations, we are able to compute several cases with and without water mist, and are able to examine droplet size and mass loading effects. Unlike the experiment, in the simulations, no venting occurs, so the simulations will not match the decay in overpressure that is seen in the experiments. For this reason we compare only the first 0.1 seconds between the experiment and the simulations. The simulations suggest a longer time may be needed to attain a true quasi-static state but the experimental data indicates that for longer times, the venting is likely to impact the measured pressure. Hence, the time, 0.1 seconds is taken as a compromise and will have some effect on the absolute quantities compared.

Other notable simplifications between the experiment and the simulation include using a spherical (instead of cylindrical) charge, only using TNT instead of using a TNT charge with a pentolite booster, and assuming all of the water is uniformly distributed within the chamber. Both the shape of the charge and the fact that the charge has a pentolite booster will only critically effect the dynamics close to the charge. It should have only a small effect away from the charge and no effect on the quasi-static pressure development. The uniform mist distribution may have a more significant impact on the pressure rise characteristics; however, at this time there are no good experimental measurements for the mist density distribution within the chamber at the time of the blast. This is an important area for further research.

6.1 Pressure Trace Characteristics

Before discussing the blast mitigation simulations, first we would like to note a few characteristics of the pressure curve. As mentioned previously, the pressure transducers in the experiment are positioned at the corners of the four walls, at approximately half the height of the ceiling. The transducers are within a box, about $\frac{1}{2}$ ft away from the actual corner. Since we are using an axisymmetric geometry in the simulations, we approximate this by looking at the pressure traces near the corner of the computational domain. They should share many characteristics, although it will not exactly replicate the pressure trace seen in the experiments.

Figure 15 shows the pressure trace from the simulation with the 5-lb blast without water mist present. We show results from a “numerical” transducer in the center of the domain and at the far corner (furthest point away from the blast). The far corner transducer is inset from the corner by 36 cm.

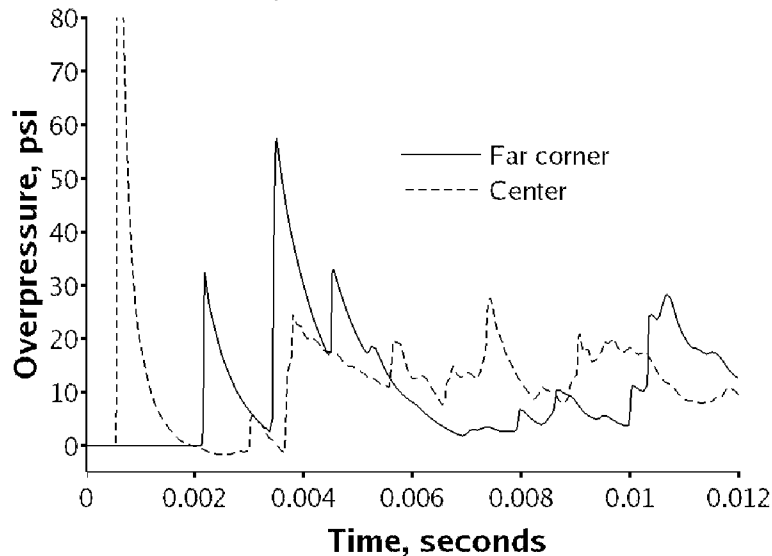


Figure 15. Blast overpressure for a 5-lb TNT charge from simulation.

The notable thing about this plot is that in the corner location, there is a group of several closely spaced pressure maxima after the front-shock arrival. This is due to the reflections occurring off of the walls surrounding the corner point. After this initial set of pressure maxima, there is a long time with minimal overpressure that lasts until almost 10 ms from the detonation of the explosive. Also of interest is that the far corner pressure trace is very different from the pressure trace in the center of the domain; which simply has one pressure spike followed by an extremely unsteady pressure trace after about 3-4 ms.

A comparison of the overpressure with mitigation and without mitigation is shown for all different charge sizes in Figure 16. For these simulations, we used a water mist mass loading of 0.5. Qualitatively, there are a few things worth noting from the figure below. The water mist mitigates the initial maximum overpressure quite significantly, reducing it by at least a factor of two. It also slows the shock wave down resulting in a later arrival time for the front-shock. Another interesting feature is that it has significantly damped the maxima in the pressure trace from 0.01 seconds onwards.

There is still an overall overpressure rise in the chamber, which is described below more quantitatively.

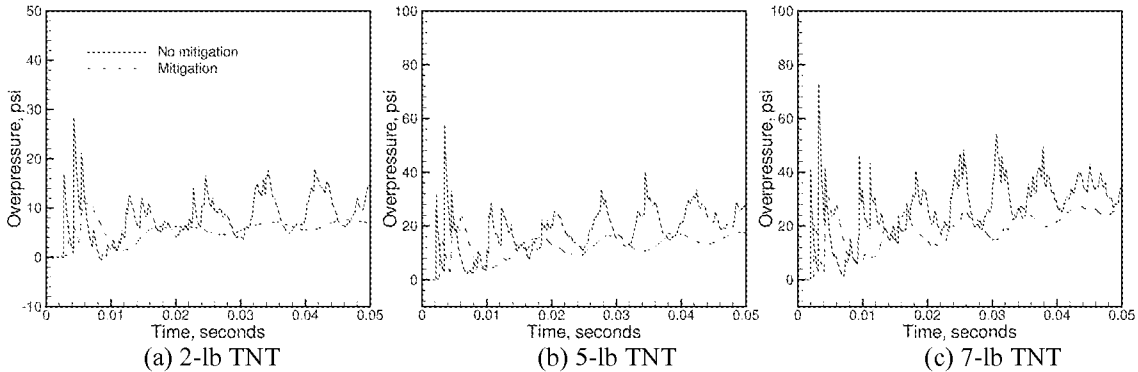


Figure 16. Pressure traces for far corner location with (dashed) and without (solid) water mist present in the domain. Water mist mass loading is 0.5 for these simulations.

6.2 Quasi-static Pressure Characteristics

Our main interest in the simulations is determining the quasi-static pressure difference with and without the water mist present. For this report, we examine three different quasi-static pressure measurements; from 0-0.05 seconds (QSP1), from 0.05-0.1 seconds (QSP2), and from 0-0.1 seconds (QSP3). These three values are selected for different reasons. The QSP1 calculation is effected by how quickly the pressure builds up within the chamber. The QSP2 calculation is significant because it is more representative of the final pressure in an enclosure that is subjected to a blast if no venting occurs. The final value from 0-0.10 is representative of the total impulse that is felt by an object at the corner location. The results are given in Table 2.

Several comments can be made first by comparing the measured quasi-static pressures shown in Table 2 with the results from the thermodynamic analysis presented earlier in Table 1. As expected, the thermodynamic analysis significantly overpredicts the overpressure within the enclosure without water mist present. This is probably because the thermodynamic procedure assumes that all the reactions go to completion, whereas realistically not all of the fuel will react for various reasons, and also some intermediate species may have high concentrations at the high temperatures. Such details are not accounted for in the simplified analysis. More interestingly, with water the thermodynamic analysis severely underpredicts the quasi-static overpressure compared with the experimental results. That is, the amount of mitigation predicted by this simple analysis is larger than that observed in the experiments. These results show how poorly a simple thermodynamic analysis is able to capture what actually happens with blast mitigation and highlights the need for more detailed numerical simulations.

The two-dimensional simulations are better at capturing the experimental quasi-static pressure, although there are some notable differences, as expected, in the absolute quantities. First, without mitigation, comparing the QSP1 value between the experiment and simulation shows the simulation almost always underpredicts this value. This may be because the secondary reactions are occurring more quickly in the experiments than in the simulation. This may also be partly due to the inherent limitation of an axisymmetric simulation where the amount of mixing is usually underestimated due to the neglect of three-dimensional effects within the flow. Interestingly, the simulations consistently

overpredict QSP2. This is perhaps due to the overly simplistic reaction kinetics, which does not account for significant quantities of stable intermediates at the elevated temperatures and pressures. These two quantities tend to balance to provide a fairly good approximation for the total impulse over the first 0.1 seconds as represented in QSP3. Furthermore, previous comparisons between the axisymmetric simulations and published experimental data on quasi-static pressures were much closer suggesting that these experimental measurements may also be on the lower side.

Unlike the thermodynamic analysis, the simulations provide a much more accurate representation of the actual mitigation seen with water mist. Again we see a similar behavior in the absolute quantities as without water mist: that is, QSP1 is typically underpredicted and QSP2 is overpredicted by the simulation, most likely due to similar circumstances as mentioned above. Finally, the simulations do show that further reduction in the quasi-static pressures can be attained by increasing the amount of water mist.

Table 2. Quasi-static pressure results for Indian Head experiments and simulations at NRL. QSP1 is averaged from $t=0$ to $t=0.05$ seconds, QSP2 is averaged from $t=0.05$ to $t=0.10$ seconds, and QSP3 is averaged from $t=0.00$ to $t=0.10$ seconds. Quasi-static pressure is in psig. Experimental data from Bailey [15].

CHARGE SIZE	QSP1	QSP2	QSP3	Comments
2 lb	9.34963	8.54686	8.93042	Experiment Channel 1
	8.5521	12.0304	10.3488	Simulation
2lb with water mist	5.85833	5.77053	5.81159	Experiment Channel 1
	5.60023	8.83787	7.23418	Simulation, mass loading 0.5
5lb	24.1847	22.9487	23.5395	Experiment 20050531 Ch 1
	23.9891	23.2634	23.6107	Experiment 20050601 Ch 1
	18.8103	26.774	22.8796	Simulation
5lb with water mist	15.4664	15.0824	15.2685	Experiment 20050531 Ch 1
	15.6416	14.8999	15.2583	Experiment 20050601 Ch 1
	15.9743	15.1832	15.5625	Experiment 20050601 Ch 1 with air
	12.4926	17.9322	15.2378	Simulation, mass loading 0.5
	6.20243	9.88448	8.05222	Simulation, mass loading 1.0

A better measure of the level of agreement between the experimental measurements and the computed values may be to consider the amount of mitigation as measured by the percentage reduction in pressures. This would remove the effect of some of the basic differences between the experimental set up and the simulations because that would impact both cases without and with water mist. Table 3 compares the water mist mitigation efficiency calculated from experimental and simulation results. The efficiency is calculated as the percent reduction in overpressure scaled by the unmitigated overpressure. This comparison suggests that the simulations do quite well at predicting the amount of mitigation that can be expected from a given scenario.

Table 3. Water-mist effectiveness, calculated by taking the difference in the quasi-static overpressure divided by the unmitigated overpressure.

CHARGE SIZE	QSP1	QSP2	QSP3	Comments
2 lb	37.3%	32.5%	34.9%	Experiment
	34.5%	26.5%	30.1%	Simulation
5 lb	36.0%	34.3%	35.1%	Experiment (20050531 results)
	33.6%	33.0%	33.4%	Simulation

Note that the numbers in the table for the experimental data are different than the 40%, 47%, and 40% quoted in [15]. The reason for this difference is that those numbers are obtained from quasi-static overpressures averaged over one second, not the 0.05 and 0.1 second shown above. Over one-second a considerable amount of venting has taken place, and therefore the numbers are not representative of an enclosed room, but of a vented room. We have chosen the 0.1 second interval because it is more representative of unvented enclosures.

7. CHALLENGES

The discussion so far has highlighted the difficulties in making accurate and adequate measurements and conducting corresponding simulations of the hostile environment around an explosion. Here we address several computational challenges that need to be addressed for improving predictions of blast mitigation in practical scenarios of interest to the Navy.

7.1 Non-TNT Explosives and Improved Detonation Model

Although TNT is useful for comparison and calibration purposes, many of the explosives used for military applications today are entirely different from TNT or are a mixture of different explosives. Therefore, it is important to have some idea of how these explosives will behave differently from TNT. Different explosives can easily be accommodated within our solution framework as explained in Section 2.4, especially since the finer details of the detonation process are only of secondary importance in these studies. We have accumulated data for a wide range of explosives, as shown in Appendix A and conducted simplified analysis with this data. Multidimensional simulations can be conducted as needed for various explosives.

Further improvement in the representation of the early stages of the explosion are required if we want a more accurate representation of the front-shock strength and arrival times. It may also become important in complex geometries where energy may be channeled between barriers in specific ways. In this case, a more accurate depiction of the detonation itself may be necessary.

7.2 Improved Droplet Modeling

For the simulations computed in this report, we have assumed very small droplets, usually less than 25-30 microns. In practice, it is difficult to generate droplets of this size along with the high mass flow rates necessary for fire and blast mitigation, although new techniques are being developed that show promise in this area. For the Marioff High-Fog system, the droplet size generated is generally much larger than the 25-30 micron range, and is often in the range of 100-200 microns. To appropriately simulate this, a breakup model needs to be implemented into the sectional approach. The difficulty in doing this is that there is very little information in the way of breakup for sub-100 micron droplets. Most of the research has focused on breakup of single, isolated droplets often in the mm size range, with a specific interest in understanding the breakup of fuel droplets. For the blast and shock wave mitigation case, these studies ignore energetics that might be important such as the extraction of energy due to the breakup process.

We have currently implemented a breakup model into the sectional approach, and have compared it with a breakup model implemented in a particle-tracking code. The two different approaches give very similar solutions for shock wave attenuation in shock tubes, giving us verification that the sectional breakup model is working correctly. We are still in the process of finding experimental results to validate our model. Once that is completed the breakup model can be implemented in the mitigation code and we can focus on larger droplets that are likely to be used in practical implementations.

7.3 Complex Three-dimensional Geometries with VCE/SS

As the blast mitigation project moves forward, simulations and experiment will be required to look at more practical scenarios. These often will include complex three-dimensional geometries. Several different approaches can be used to address these complexities. Body-fitted structured meshes have been used in the past quite extensively, but are difficult to produce, especially as obstructions are added to the domain.

Unstructured grids are attractive since automated algorithms can be written to produce grids subject to specific constraints. The approach we are currently investigating is called the virtual-cell-embedding with surface segments (VCE/SS) method. This method is based on the virtual cell embedding (VCE) method of Landsberg and Boris [31], and keeps the uniform structured mesh. VCE determines which cells are completely blocked, and which cells are only partially blocked. It then computes the partial volume and partial interface surfaces needed by the transport algorithm based on a grid embedded within each partially blocked cell. Surface segments adds the ability to have additional cell interface surfaces for the partially blocked cells besides the common 4 or 6 for structured meshes. The additional surfaces can have fluxes or other surface forces associated with them. This VCE/SS method is currently integrated into a 3D FCT algorithm. As a demonstration of the ability, we show a blast solution without mitigation in an axisymmetric geometry with four cylinders and a ramp computed using the VCE/SS method in Figure 17.



Figure 17. Two snapshots of the magnitude of the gradient of density for the VCE/SS test case, an axisymmetric geometry with four cylinders and a ramp. Snapshots are at 70 ms (left) and 100 ms (right).

7.4 Parallel Adaptive Mesh Refinement using PARAMESH

In addition to doing complex geometries and obstructions using the VCE/SS technique, unsteady simulations with well-resolved shocks in three-dimensional environments require some sort of adaptive grid technology to be practical. For instance, the grid used for the axisymmetric simulations is 500x500, and represents a good compromise between efficiency and resolution. Halving the resolution significantly dampens the shocks, while doubling the resolution only slightly increases the accuracy while slowing down the solution procedure by at least a factor of four. To extend this to three dimensions, a 500x500x500 grid would have 125 million grid cells. Even with the supercomputers of today, it is prohibitively expensive to do this many cells for a long duration, time-accurate calculation. Adaptive mesh refinement allows us to pack cells where they are needed (near the shock waves and reaction zones), while leaving the grid fairly coarse in other areas. We have selected PARAMESH for parallel adaptive mesh refinement [32].

PARAMESH works by defining a base mesh block size, for example 16x16x16 cells, and constructing the mesh from these base mesh blocks. Each mesh block can be refined if it meets refinement criteria into 4 or 8 (for 2d or 3d simulations) child mesh blocks, doubling the effective resolution within the original parent block. Groups of 4 or 8 mesh blocks can also be derefined if the solution meets specific criteria. Each mesh block exists on a single processor and communication between the mesh blocks occurs through the PARAMESH library using MPI calls.

An example of the blast calculation using the PARAMESH libraries is shown in Figure 18, where we detonate 5 lbs of TNT in a 215 cm x 215 cm cylinder. Temperature is shown in the figure, both with and without the mesh. There are five levels of refinement in this calculation, with each block having a 16x16 mesh. Here we used both the density and the temperature gradients to determine which areas to refine and derefine. This captures both the reflected front shock wave and the intricate reaction-front structure. For this example, we have set the base resolution for the domain at 64x64, resulting in a 3.36 cm resolution. From there, we refine five levels to a 1.05 mm resolution, only in locations where it is needed. As the flow develops, the grid is adapted to properly resolve the shock-front and reaction-front. For the snapshot shown in Figure 18, we have 4960 base blocks, which corresponds to 1.27 million cells. For a uniform 1.05 mm resolution, we would need 4.19 million grid cells.

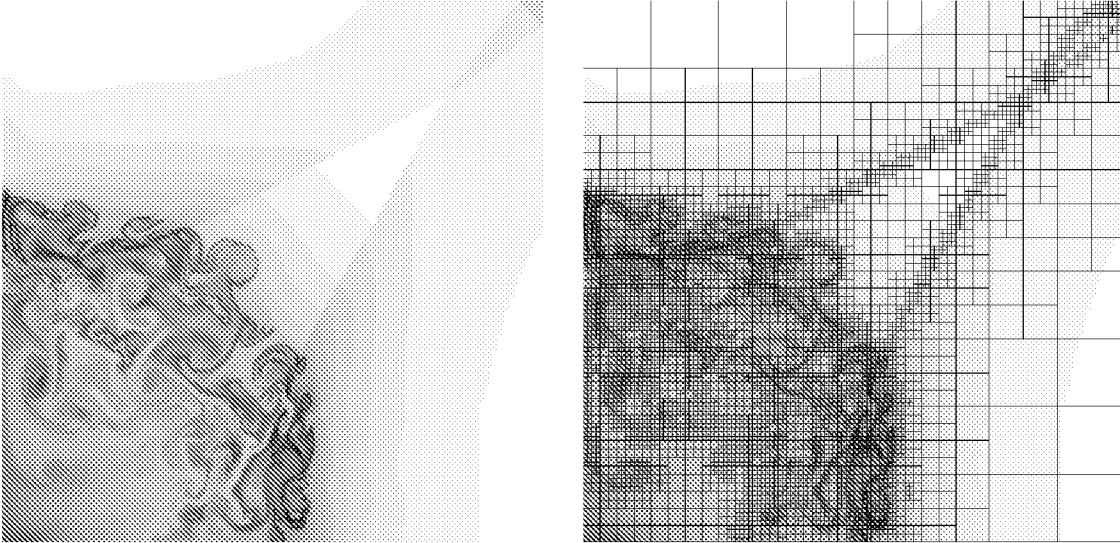


Figure 18. Temperature solution with PARAMESH/BLAST code (FBX2), with (left) and without (right) grid. 2.273 kg TNT in a 215x215 cm domain. 16x16 base mesh size. 5 levels of refinement.

7.5 Fluid-Structure Interactions

Another area of importance is in the interaction between the gas-flow and structural elements. The surrounding walls and other structures can absorb a significant amount of the energy related to the blast, and in doing so change the basic pressure development within an enclosed area. In addition to the steel structure, protective jackets or coatings can be applied to especially vulnerable areas that may absorb much of the blast energy without causing damage to the overall structure. For the current experiments, fluid-structure interaction has not been critical, however, for practical Navy applications, this component will be important in determining the amount of damage sustained by a blast. Furthermore, the basic knowledge gained from our studies can be used to design effective multimaterial solutions tailored to protect specific high value assets.

8. CONCLUSIONS

This report is the third in a series of reports that have dealt with simulating mitigation of confined and unconfined blasts. To date, these simulations have examined mitigation using water mist. We have, however, remained flexible in our approach so that we can incorporate other mitigation techniques that show promise. The report has briefly outlined the numerical procedure used for the simulations and then focused on a series of calculations that have elucidated both qualitative and quantitative features of blast mitigation using water mist.

The first set of simulations examined the multi-dimensional nature of the expanding shock-front and reaction-front after detonation of the explosive. It was found that the reaction-front for blasts typically lags considerably behind the shock-front except for close to the explosive. Water mist is pushed outwards away from the explosive location by the shock front and shocked air gases, and typically does not penetrate into the reaction front except close to the explosive. Because of this, water mist does not directly suppress the secondary reactions in an unconfined explosion. For oxygen-

deficient explosives such as TNT, pressure development in an enclosure is tied closely to heat release from the oxidation of excess fuel in the reaction-front, which tends to be mixing controlled. Although there is no coupling between the shock-front and reaction-front, shock waves reflected off of the walls in the enclosure drive mixing and thus reactions in the reaction-front.

The second series of mitigation simulations examined the effect of water mist of the shock-front for unconfined blasts. Several interesting conclusions can be derived from these results. First, droplet size appears to play a secondary role when compared to the mass loading for shock-front mitigation. Closer to the explosive, smaller water droplets are actually less effective at mitigation, while further downstream there seems to be an optimum size dependent on the mass loading. Vaporization also appears to have very little effect on the mitigation of the shock front, particularly close to the explosive, suggesting that momentum extraction plays the key role in mitigation of the shock front. It also appears that the mitigation experienced by an observer at a given distance from an explosive is due to the total water mass between the observer and the explosive. It does not matter if the water is concentrated near the explosive or spread out between the explosive and observer. As long as the total mass is the same, the amount of mitigation will be similar. This suggests that water-blankets may be as effective as general water mist so long as the amount of water used is similar.

The next set of simulations examined general characteristics of the mitigation of quasi-static pressure buildup within an enclosure. Two general conclusions can be drawn from these simulations. First, water mist appears to affect the amount of mixing between oxidizer and excess fuels by decreasing the magnitude of the instabilities that develop within the reaction-front, and also by reducing the strength of the reflected shock waves that help to drive the mixing. Water mist does not appear, however, to extinguish the secondary reactions, therefore we do not see the very large amounts of mitigation that are theoretically possible. Simulations also tested the effect of different wall boundary conditions for the mist (a sticky versus a reflective wall), and interestingly found that the water mist wall boundary condition had only a small effect on the actual mitigation.

The final set of simulations were done in support of experiments conducted by NRL at the Naval Surface Warfare Center (Indian Head). A simple thermodynamic analysis was first compared with the experiments, and severely underpredicted the mitigated quasi-static pressure, thus overpredicting the mitigation efficiency and demonstrating how poor this method is for these cases. Unsteady axisymmetric simulations tended to overpredict the absolute values for the quasi-static pressure both with and without water mist present, most likely because various loss mechanisms (incomplete combustion, absorption of energy by walls and other structures, and venting) that were not incorporated into the model. However, the simulations were able to predict the overall mitigation efficiency of the water mist to within a few percent. This suggests that an unsteady multidimensional simulation is essential in determining what type of mitigation to expect. This will be particularly true when examining more complex spaces and mitigation strategies.

The current results have shown that the simulation approach can give both useful predictions and trends for shock-front and quasi-static mitigation. Validation using data from [15] has helped to ensure that the present physical models are realistic and not missing essential physics necessary for the computation. The simulations have also

helped to elucidate some of the general characteristics of these explosive blasts, as well as the main mechanisms behind both the shock-front and quasi-static mitigation. The current focus of the research is on further improving the efficiency and accuracy of the simulation code for use as a general tool that the Navy and DoD can use for evaluating blast mitigation strategies for ships and other areas of general interest.

Acknowledgements

This work was sponsored by the Office of Naval Research, primarily through NRL 6.1 Computational Physics Task Area, with additional support through Code 334 Damage Control Task.

References

1. Kailasanath, K., Tatem, P.A., Williams, F.W., and Mawhinney, J. "Blast Mitigation Using Water --- A Status Report." NRL Technical Report NRL/MR/6410--02-8606, Naval Research Lab, 2002.
2. Liu, M.B., Liu, G.R., and Lam, K.Y. "Investigations into Water Mitigation using a Meshless Particle Method." *Shock Waves*, 12: 181-185, 2002.
3. Catlin, C. "Passive explosion suppression by blast-induced atomisation from water containers." *J. Hazard. Mat.*, A94(2): 103-132, 2002.
4. Buzukov, A.A. "Decreasing the Parameters of an Air Shock Using an Air-Water Curtain." *Combust. Explosion and Shock Waves*, 36: 395-404, 2000.
5. van Wingerden, K. "Mitigation of gas explosions using water deluge." *Process Safety Progress*, 19: 173-178, 2000.
6. Thomas, G.O. "On the conditions required for explosion mitigation by water sprays." *Trans. IChemE*, 78: 339-354, 2000.
7. Darwin, R.L. and Williams, F.W. "The development of water mist fire protection systems for US Navy ships." *Naval Engineers J.*, 112:49-57, 2000.
8. Prasad, K., Li, C., Kailasanath, K., Ndubizu, C., Ananth, R., and Tatem, P. "Numerical modeling of water mist suppression of methane-air diffusion flames." *Combust. Sci. and Tech.*, 132:325-364, 1998.
9. Prasad, K., Li, C., and Kailasanath, K. "Optimizing water mist injection characteristics for suppression of co-flow diffusion flames." *Proceedings of the Combustion Institute*, 27: 2847-2855, 1998.
10. Prasad, K., Li, C. and Kailasanath, K. "Simulation of water mist suppression of small scale methanol liquid pool fires." *Fire Safety Journal*, 33:185-212, 1999.
11. Schwer, D.A. and Kailasanath, K. "Blast Mitigation by Water Mist 1) Simulation of Confined Blast Waves." NRL Technical Report NRL/MR/6410—02-8636, Naval Research Lab, 2002.
12. Schwer, D.A. and Kailasanath, K. "Blast Mitigation by Water Mist 2) Shock Wave Mitigation Using Glass Particles and Water Droplets in Shock Tubes." NRL Technical Report NRL/MR/6410—03-8658, Naval Research Lab, 2003.
13. Schwer, D.A. and Kailasanath, K. "Mitigation of Blast Waves From Explosives using Water Mist," in *Proceedings of the Third Joint Meeting of the US Sections of the Combustion Institute*, Chicago, IL, Mar. 16-19, 2003.
14. Schwer, D.A. and Kailasanath, K. "Mitigation of Blasts Using Water Mist," in *31st DDES Explosives Safety Seminar Proceedings*, San Antonio, TX, Aug 24-26, 2004.
15. Bailey, J.L., Farley, J.P., Williams, F.W., Lindsay, M.S., Schwer, D.A., "Blast Mitigation Using Water Mist." NRL Technical Report NRL/MR/6180—06-8933, Naval Research Lab, 2006.
16. Tambour, Y. "Vaporization of polydisperse fuel sprays in a laminar boundary layer flow: A sectional approach." *Combust. Flame*, 58:103-114, 1984.
17. Tambour, Y. "A Lagrangian sectional approach for simulating droplet size distribution of

- vaporizing fuel sprays in a turbulent jet.” *Combust. Flame*, 60:15-28, 1985.
18. Tambour, Y. “Derivation of near-field sectional equations for the dynamics of polydisperse spray flows: An analysis of the relaxation zone behind a normal shock wave.” *Combust. Flame*, 95:383-409, 1993.
19. Greenberg, J.B., Silverman, I., and Tambour, Y. “On the origins of spray sectional conservation equations.” *Combust. Flame*, 93:90-96, 1993.
20. Laurent, F. and Massot, M. “Multi-fluid modelling of laminar polydisperse spray flames: origin, assumptions and comparison of sectional and sampling methods.” *Combust. Theory Modelling*, 5:537-572, 2001.
21. Clift, R., Grace, J.R., and Weber, M.E. *Bubbles, Drops, and Particles*. Academic, New York, 1978.
22. Ranz, W.E. and Marshall, W.R. “Evaporation from drops.” *Chem. Engrg. Prog.*, 48(3): 141-173, 1952.
23. Keenan, J.H. *Steam Tables*. Wiley, New York, 1979.
24. Boris, J.P. and Book, D.L. “Flux Corrected Transport I. SHASTA, A fluid transport algorithm that works.” *J. Comput. Phys.*, 11(1):38-69, 1973.
25. Boris, J.P., Landsberg, A.M., Oran, E.S., and Gardner, J.H. “LCPFCT—A Flux-Corrected Transport algorithm for solving generalized continuity equations.” NRL Technical Report NRL/MR/6410—93-7192, Naval Research Lab, 1993.
26. Agrawal, G., Sussman, A., and Saltz, J. “An integrated runtime and compile-time approach for parallelizing structured and block structured applications.” *IEEE Transactions on Parallel and Distributed Systems*, 6(7): 747-754, 1995.
27. Keenan, W.A. and Wager, P.C. “Mitigation of confined explosion effects by placing water in proximity of explosives.” In *25th DoD Explosives Safety Seminar*, Anaheim, CA August 18-20, 1992.
28. www.hi-fog.com.
29. Kinney, G.F. and Graham, K.J. *Explosive Shocks in Air*. Springer-Verlag, Berlin, 1985.
30. Cooper, P.W. *Explosives Engineering*. Wiley-VCH, New York, NY, 1996.
31. Landsberg, A.M. and Boris, J.P., AIAA Paper No. 97-1982, 1997.
32. MacNeice, P., Olson, K.M., Mobarry, C., deFainchtein, R. and Packer, C. *Comp Phys Commun*, Vol 126, pp. 330-354, 2000.
33. Mader, C.L. *Numerical Modeling of Explosives and Propellants*. CRC Press, Boca Raton, FL, 1998.

APPENDIX A. Explosive Decomposition

Although there are many, many, different types of explosives, most common explosives have the same basic constituents (carbon, nitrogen, oxygen, and hydrogen), and can be represented as $C_aH_bN_cO_d$, and produce similar product gases after detonation. Given heats of formation of individual explosives, estimates can be made of the heat of detonation and the heat of combustion (includes heat released from secondary reaction) assuming a hierarchy of decomposition. The hierarchy we choose for explosive decomposition for a general explosive:

1. All nitrogen goes to N_2
2. Hydrogen combines with available oxygen to form H_2O .
3. Carbon combines with any remaining oxygen to form CO .
4. Carbon monoxide combines with any remaining oxygen to form CO_2 .
5. Aluminum combines with any remaining oxygen to form Al_2O_3 .
6. Any remaining oxygen forms O_2 .
7. Any remaining carbon forms $C(s)$ (graphite dust).

We have added in the Aluminum because of its presence in many metalized explosives, however, the role it plays in the detonation is unclear and the subject of much research. Note that other hierarchies may be applied; in particular, some researchers prefer to react the carbon to carbon dioxide without a carbon monoxide intermediate. However, this hierarchy appears to give better results for most detonation energies except in the case of RDX. Considerable research has also been done to determine the exact detonation products for some explosives, for instance see Mader [32:mader98]. Where this data is available and reliable it is good to use, however, for more general considerations the above hierarchy can be used. Table 1 shows the results for some common explosives using this hierarchy.

In addition to pure explosives, we also consider the decomposition and reaction of TNT-castable explosives in Table 2. Note that this thermodynamic treatment only gives the heat release and products for the detonation and combustion of an explosive. We do not attempt to provide any other detonation information (such as detonation speed and pressure). For our purposes, with our relatively simple initial condition, this information is all that is needed.

Table A1. List of pure explosives, with global detonation and combustion reactions.
All specie products are in gm-moles.

1 kg TNT (4.40276 gm-mol, C₇H₅N₃O₆)
 1 kg TNT => 11.0069 H₂O(l) + 15.4097 C(s) + 15.4097 CO + 6.60415 N₂ + 1088.65 kcal
 1 kg TNT + 23.1145 O₂ => 11.0069 H₂O(l) + 30.8194 CO₂ + 6.60415 N₂ + 3580.4 kcal

1 kg HMX (3.3761 gm-mol, C₄H₈N₈O₈)
 1 kg HMX => 13.5044 H₂O(l) + 13.5044 CO + 13.5044 N₂ + 1339.92 kcal
 1 kg HMX + 6.75219 O₂ => 13.5044 H₂O(l) + 13.5044 CO₂ + 13.5044 N₂ + 2253.35 kcal

1 kg RDX (4.50248 gm-mol, C₃H₆N₆O₆)
 1 kg RDX => 13.5074 H₂O(l) + 13.5074 CO + 13.5074 N₂ + 1345.9 kcal
 1 kg RDX + 6.75371 O₂ => 13.5074 H₂O(l) + 13.5074 CO₂ + 13.5074 N₂ + 2259.55 kcal

1 kg Ammonium Picrate (4.06339 gm-mol, C₆H₆N₄O₇)
 1 kg AP => 12.1902 H₂O(l) + 8.12678 C(s) + 16.2536 CO + 8.12678 N₂ + 880.293 kcal
 1 kg AP + 16.2536 O₂ => 12.1902 H₂O(l) + 24.3803 CO₂ + 8.12678 N₂ + 2744.09 kcal

1 kg Ammonium Nitrate (12.4933 gm-mol, NH₄NO₃)
 1 kg AN => 24.9866 H₂O(l) + 6.24664 O₂ + 12.4933 N₂ + 616.648 kcal
 1 kg AN => 24.9866 H₂O(l) + 6.24664 O₂ + 12.4933 N₂ + 616.648 kcal

1 kg PETN (3.16256 gm-mol, C₅H₈N₄O₁₂)
 1 kg PETN => 12.6502 H₂O(l) + 6.32511 CO + 9.48767 CO₂ + 6.32511 N₂ + 1516.7 kcal
 1 kg PETN + 3.16256 O₂ => 12.6502 H₂O(l) + 15.8128 CO₂ + 6.32511 N₂ + 1944.53 kcal

1 kg EDNA (6.66267 gm-mol, C₂H₆N₄O₄)
 1 kg EDNA => 19.988 H₂O(l) + 6.66267 C(s) + 6.66267 CO + 13.3253 N₂ + 1380.71 kcal
 1 kg EDNA + 9.994 O₂ => 19.988 H₂O(l) + 13.3253 CO₂ + 13.3253 N₂ + 2458.06 kcal

1 kg Tetryl (3.48262 gm-mol, C₇H₅N₅O₈)
 1 kg Tetryl => 8.70655 H₂O(l) + 5.22393 C(s) + 19.1544 CO + 8.70655 N₂ + 1117.14 kcal
 1 kg Tetryl + 14.8011 O₂ => 8.70655 H₂O(l) + 24.3784 CO₂ + 8.70655 N₂ + 2904.11 kcal

1 kg HNS (2.22074 gm-mol, C₁₄H₆N₆O₁₂)
 1 kg HNS-I => 6.66223 H₂O(l) + 11.1037 C(s) + 19.9867 CO + 6.66223 N₂ + 1024.72 kcal
 1 kg HNS-I + 21.097 O₂ => 6.66223 H₂O(l) + 31.0904 CO₂ + 6.66223 N₂ + 3421.04 kcal

1 kg TATB (3.87372 gm-mol, C₆H₆N₆O₆)
 1 kg TATB => 11.6212 H₂O(l) + 11.6212 C(s) + 11.6212 CO + 11.6212 N₂ + 958.218 kcal
 1 kg TATB + 17.4317 O₂ => 11.6212 H₂O(l) + 23.2423 CO₂ + 11.6212 N₂ + 2837.36 kcal

Table A2. List of TNT castable explosives, with global detonation and combustion reactions. All specie products are in gm-moles. Explosive compositions are taken from [28:cooper96].

1 kg of Ammonal:

0.67 kg (2.94985 gm-mol) TNT (C₇H₅N₃O₆)
 0.11 kg (4.07709 gm-mol) Aluminum (Al)
 0.22 kg (2.74852 gm-mol) Ammonium Nitrate (NH₄NO₃)
 1 kg Ammonal => 12.8717 H₂O(l) + 7.57596 C(s) + 13.073 CO + 7.1733 N₂ + 4.07709 Al(s) + 937.674 kcal
 1 kg Ammonal + 20.2281 O₂ => 12.8717 H₂O(l) + 20.649 CO₂ + 7.1733 N₂ + 2.03855 Al₂O₃ + 3350.99 kcal

1 kg of Amatol (a):

0.6 kg (2.64166 gm-mol) TNT (C₇H₅N₃O₆)
 0.4 kg (4.99731 gm-mol) Ammonium Nitrate (NH₄NO₃)
 1 kg Amatol (a) => 16.5988 H₂O(l) + 4.24849 C(s) + 14.2431 CO + 8.9598 N₂ + 1031.88 kcal
 1 kg Amatol (a) + 11.3701 O₂ => 16.5988 H₂O(l) + 18.4916 CO₂ + 8.9598 N₂ + 2394.9 kcal

1 kg of Amatol (b):

0.5 kg (2.20138 gm-mol) TNT (C₇H₅N₃O₆)
 0.5 kg (6.24664 gm-mol) Ammonium Nitrate (NH₄NO₃)
 1 kg Amatol (b) => 17.9967 H₂O(l) + 1.4582 C(s) + 13.9515 CO + 9.54872 N₂ + 1017.69 kcal
 1 kg Amatol (b) + 8.43394 O₂ => 17.9967 H₂O(l) + 15.4097 CO₂ + 9.54872 N₂ + 2098.52 kcal

1 kg of Amatol (c):

0.2 kg (0.880553 gm-mol) TNT (C₇H₅N₃O₆)
 0.8 kg (9.99463 gm-mol) Ammonium Nitrate (NH₄NO₃)
 1 kg Amatol (c) => 22.1906 H₂O(l) + 6.16387 CO₂ + 0.374411 O₂ + 11.3155 N₂ + 1209.4 kcal
 1 kg Amatol (c) => 22.1906 H₂O(l) + 6.16387 CO₂ + 0.374411 O₂ + 11.3155 N₂ + 1209.4 kcal

1 kg of Comp B:

0.36 kg (1.585 gm-mol) TNT (C₇H₅N₃O₆)
 0.63 kg (2.83656 gm-mol) RDX (C₃H₆N₆O₆)
 0.01 kg (0.0147732 gm-mol) Wax (C₁₅H₃₁COOC30H₆₁)
 1 kg Comp B => 13.1517 H₂O(l) + 6.87707 C(s) + 13.4071 CO + 10.8872 N₂ + 1269.09 kcal
 1 kg Comp B + 13.5806 O₂ => 13.1517 H₂O(l) + 20.2842 CO₂ + 10.8872 N₂ + 2822.81 kcal

1 kg of Comp B-2:

0.4 kg (1.76111 gm-mol) TNT (C₇H₅N₃O₆)
 0.55 kg (2.47636 gm-mol) RDX (C₃H₆N₆O₆)
 0.05 kg (0.0738662 gm-mol) Wax (C₁₅H₃₁COOC30H₆₁)
 1 kg Comp B-2 => 15.2297 H₂O(l) + 12.8118 C(s) + 10.3428 CO + 10.0707 N₂ + 1321.97 kcal
 1 kg Comp B-2 + 17.9832 O₂ => 15.2297 H₂O(l) + 23.1547 CO₂ + 10.0707 N₂ + 3226.65 kcal

1 kg of Comp B-3:

0.4 kg (1.76111 gm-mol) TNT (C₇H₅N₃O₆)
 0.6 kg (2.70149 gm-mol) RDX (C₃H₆N₆O₆)
 1 kg Comp B-3 => 12.5072 H₂O(l) + 6.16387 C(s) + 14.2683 CO + 10.7461 N₂ + 1243 kcal
 1 kg Comp B-3 + 13.298 O₂ => 12.5072 H₂O(l) + 20.4322 CO₂ + 10.7461 N₂ + 2787.89 kcal

1 kg of Cyclotol (a):

0.5 kg (2.20138 gm-mol) TNT (C₇H₅N₃O₆)
 0.5 kg (2.25124 gm-mol) RDX (C₃H₆N₆O₆)
 1 kg Cyclotol (a) => 12.2572 H₂O(l) + 7.70484 C(s) + 14.4586 CO + 10.0558 N₂ + 1217.28 kcal
 1 kg Cyclotol (a) + 14.9341 O₂ => 12.2572 H₂O(l) + 22.1634 CO₂ + 10.0558 N₂ + 2919.97 kcal

1 kg of Cyclotol (b):

0.35 kg (1.54097 gm-mol) TNT (C₇H₅N₃O₆)
 0.65 kg (2.92661 gm-mol) RDX (C₃H₆N₆O₆)
 1 kg Cyclotol (b) => 12.6322 H₂O(l) + 5.39339 C(s) + 14.1732 CO + 11.0913 N₂ + 1255.86 kcal
 1 kg Cyclotol (b) + 12.48 O₂ => 12.6322 H₂O(l) + 19.5666 CO₂ + 11.0913 N₂ + 2721.85 kcal

1 kg of Cyclotol (c):

0.3 kg (1.32083 gm-mol) TNT (C₇H₅N₃O₆)

0.7 kg (3.15173 gm-mol) RDX (C₃H₆N₆O₆)

1 kg Cyclotol (c) => 12.7573 H₂O(l) + 4.6229 C(s) + 14.0781 CO + 11.4364 N₂ + 1268.73 kcal

1 kg Cyclotol (c) + 11.662 O₂ => 12.7573 H₂O(l) + 18.701 CO₂ + 11.4364 N₂ + 2655.8 kcal

1 kg of Cyclotol (d):

0.25 kg (1.10069 gm-mol) TNT (C₇H₅N₃O₆)

0.75 kg (3.37686 gm-mol) RDX (C₃H₆N₆O₆)

1 kg Cyclotol (d) => 12.8823 H₂O(l) + 3.85242 C(s) + 13.983 CO + 11.7816 N₂ + 1281.59 kcal

1 kg Cyclotol (d) + 10.8439 O₂ => 12.8823 H₂O(l) + 17.8354 CO₂ + 11.7816 N₂ + 2589.76 kcal

1 kg of DBX:

0.4 kg (1.76111 gm-mol) TNT (C₇H₅N₃O₆)

0.18 kg (6.67161 gm-mol) Aluminum (Al)

0.21 kg (2.62359 gm-mol) Ammonium Nitrate (NH₄NO₃)

0.21 kg (0.94552 gm-mol) RDX (C₃H₆N₆O₆)

1 kg DBX => 12.4865 H₂O(l) + 3.54028 C(s) + 11.624 CO + 8.10181 N₂ + 6.67161 Al(s) + 916.911 kcal

1 kg DBX + 19.3597 O₂ => 12.4865 H₂O(l) + 15.1643 CO₂ + 8.10181 N₂ + 3.3358 Al₂O₃ + 3372.19 kcal

1 kg of Ednatol:

0.45 kg (1.98124 gm-mol) TNT (C₇H₅N₃O₆)

0.55 kg (3.66447 gm-mol) EDNA (C₂H₆N₄O₄)

1 kg Ednatol => 15.9465 H₂O(l) + 10.5988 C(s) + 10.5988 CO + 10.3008 N₂ + 1249.28 kcal

1 kg Ednatol + 15.8982 O₂ => 15.9465 H₂O(l) + 21.1976 CO₂ + 10.3008 N₂ + 2963.12 kcal

1 kg of HTA-3 contains:

0.29 kg (1.2768 gm-mol) TNT (C₇H₅N₃O₆)

0.22 kg (8.15419 gm-mol) Aluminum (Al)

0.49 kg (1.65429 gm-mol) HMX (C₄H₈N₈O₈)

1 kg HTA-3 => 9.80916 H₂O(l) + 4.46881 C(s) + 11.086 CO + 8.53235 N₂ + 8.15419 Al(s) + 972.267 kcal

1 kg HTA-3 + 22.2431 O₂ => 9.80916 H₂O(l) + 15.5548 CO₂ + 8.53235 N₂ + 4.07709 Al₂O₃ + 3775.38 kcal

1 kg of Minol-2:

0.4 kg (1.76111 gm-mol) TNT (C₇H₅N₃O₆)

0.2 kg (7.4129 gm-mol) Aluminum (Al)

0.4 kg (4.99731 gm-mol) Ammonium Nitrate (NH₄NO₃)

1 kg Minol-2 => 14.3974 H₂O(l) + 1.16656 C(s) + 11.1612 CO + 7.63897 N₂ + 7.4129 Al(s) + 814.149 kcal

1 kg Minol-2 + 17.8665 O₂ => 14.3974 H₂O(l) + 12.3277 CO₂ + 7.63897 N₂ + 3.70645 Al₂O₃ + 3163.29 kcal

1 kg of Octol (a):

0.23 kg (1.01264 gm-mol) TNT (C₇H₅N₃O₆)

0.77 kg (2.59959 gm-mol) HMX (C₄H₈N₈O₈)

1 kg Octol (a) => 12.93 H₂O(l) + 3.54423 C(s) + 13.9426 CO + 11.9173 N₂ + 1282.12 kcal

1 kg Octol (a) + 10.5155 O₂ => 12.93 H₂O(l) + 17.4868 CO₂ + 11.9173 N₂ + 2558.57 kcal

1 kg of Octol (b):

0.25 kg (1.10069 gm-mol) TNT (C₇H₅N₃O₆)

0.75 kg (2.53207 gm-mol) HMX (C₄H₈N₈O₈)

1 kg Octol (b) => 12.88 H₂O(l) + 3.85242 C(s) + 13.9807 CO + 11.7793 N₂ + 1277.1 kcal

1 kg Octol (b) + 10.8428 O₂ => 12.88 H₂O(l) + 17.8331 CO₂ + 11.7793 N₂ + 2585.12 kcal

1 kg of Octol (c):

0.3 kg (1.32083 gm-mol) TNT (C₇H₅N₃O₆)

0.7 kg (2.36327 gm-mol) HMX (C₄H₈N₈O₈)

1 kg Octol (c) => 12.7551 H₂O(l) + 4.6229 C(s) + 14.076 CO + 11.4343 N₂ + 1264.54 kcal

1 kg Octol (c) + 11.6609 O₂ => 12.7551 H₂O(l) + 18.6989 CO₂ + 11.4343 N₂ + 2651.47 kcal

1 kg of Pentolite (a):

0.5 kg (2.20138 gm-mol) TNT (C₇H₅N₃O₆)

0.5 kg (1.58128 gm-mol) PETN (C₅H₈N₄O₁₂)

1 kg Pentolite (a) => 11.8286 H₂O(l) + 2.96101 C(s) + 20.3551 CO + 6.46463 N₂ + 1107.14 kcal

1 kg Pentolite (a) + 13.1385 O₂ => 11.8286 H₂O(l) + 23.3161 CO₂ + 6.46463 N₂ + 2762.47 kcal

1 kg of Pentolite (b):

0.9 kg (3.96249 gm-mol) TNT (C₇H₅N₃O₆)

0.1 kg (0.316256 gm-mol) PETN (C₅H₈N₄O₁₂)

1 kg Pentolite (b) => 11.1712 H₂O(l) + 12.9199 C(s) + 16.3988 CO + 6.57624 N₂ + 1092.35 kcal

1 kg Pentolite (b) + 21.1193 O₂ => 11.1712 H₂O(l) + 29.3187 CO₂ + 6.57624 N₂ + 3416.81 kcal

1 kg of Picratol:

0.48 kg (2.11333 gm-mol) TNT (C₇H₅N₃O₆)

0.52 kg (2.11296 gm-mol) Ammonium Picrate (C₆H₆N₄O₇)

1 kg Picratol => 11.6222 H₂O(l) + 11.6226 C(s) + 15.8485 CO + 7.39592 N₂ + 980.304 kcal

1 kg Picratol + 19.5468 O₂ => 11.6222 H₂O(l) + 27.4711 CO₂ + 7.39592 N₂ + 3145.52 kcal

1 kg of PTX-1:

0.2 kg (0.880553 gm-mol) TNT (C₇H₅N₃O₆)

0.3 kg (1.35074 gm-mol) RDX (C₃H₆N₆O₆)

0.5 kg (1.74131 gm-mol) Tetryl (C₇H₅N₅O₈)

1 kg PTX-1 => 10.6069 H₂O(l) + 5.6939 C(s) + 16.7114 CO + 9.72634 N₂ + 1180.07 kcal

1 kg PTX-1 + 14.0496 O₂ => 10.6069 H₂O(l) + 22.4053 CO₂ + 9.72634 N₂ + 2846 kcal

1 kg of PTX-2:

0.31 kg (1.36486 gm-mol) TNT (C₇H₅N₃O₆)

0.27 kg (0.85389 gm-mol) PETN (C₅H₈N₄O₁₂)

0.42 kg (1.89104 gm-mol) RDX (C₃H₆N₆O₆)

1 kg PTX-2 => 12.5008 H₂O(l) + 2.21533 C(s) + 17.2812 CO + 9.42819 N₂ + 1206.68 kcal

1 kg PTX-2 + 10.8559 O₂ => 12.5008 H₂O(l) + 19.4966 CO₂ + 9.42819 N₂ + 2583.96 kcal

1 kg of Tetrytol (a):

0.2 kg (0.880553 gm-mol) TNT (C₇H₅N₃O₆)

0.8 kg (2.7861 gm-mol) Tetryl (C₇H₅N₅O₈)

1 kg Tetrytol (a) => 9.16663 H₂O(l) + 7.26108 C(s) + 18.4055 CO + 8.28607 N₂ + 1111.44 kcal

1 kg Tetrytol (a) + 16.4638 O₂ => 9.16663 H₂O(l) + 25.6666 CO₂ + 8.28607 N₂ + 3039.37 kcal

1 kg of Tetrytol (b):

0.25 kg (1.10069 gm-mol) TNT (C₇H₅N₃O₆)

0.75 kg (2.61197 gm-mol) Tetryl (C₇H₅N₅O₈)

1 kg Tetrytol (b) => 9.28164 H₂O(l) + 7.77037 C(s) + 18.2182 CO + 8.18095 N₂ + 1110.02 kcal

1 kg Tetrytol (b) + 16.8795 O₂ => 9.28164 H₂O(l) + 25.9886 CO₂ + 8.18095 N₂ + 3073.18 kcal

1 kg of Tetrytol (c):

0.3 kg (1.32083 gm-mol) TNT (C₇H₅N₃O₆)

0.7 kg (2.43784 gm-mol) Tetryl (C₇H₅N₅O₈)

1 kg Tetrytol (c) => 9.39666 H₂O(l) + 8.27966 C(s) + 18.031 CO + 8.07583 N₂ + 1108.59 kcal

1 kg Tetrytol (c) + 17.2952 O₂ => 9.39666 H₂O(l) + 26.3107 CO₂ + 8.07583 N₂ + 3107 kcal

1 kg of Tetrytol (d):

0.35 kg (1.54097 gm-mol) TNT (C₇H₅N₃O₆)

0.65 kg (2.2637 gm-mol) Tetryl (C₇H₅N₅O₈)

1 kg Tetrytol (d) => 9.51168 H₂O(l) + 8.78894 C(s) + 17.8438 CO + 7.97071 N₂ + 1107.17 kcal

1 kg Tetrytol (d) + 17.7108 O₂ => 9.51168 H₂O(l) + 26.6327 CO₂ + 7.97071 N₂ + 3140.81 kcal

1 kg of Tritonal:

0.8 kg (3.52221 gm-mol) TNT ($C_7H_5N_3O_6$)

0.2 kg (7.4129 gm-mol) Aluminum (Al)

1 kg Tritonal \Rightarrow 8.80553 $H_2O(l)$ + 12.3277 C(s) + 12.3277 CO + 5.28332 N_2 + 7.4129 Al(s) + 870.92 kcal

1 kg Tritonal + 29.611 $O_2 \Rightarrow$ 8.80553 $H_2O(l)$ + 24.6555 CO_2 + 5.28332 N_2 + 3.70645 Al_2O_3 + 4348.79 kcal

1 kg of Torpex:

0.405 kg (1.78312 gm-mol) TNT ($C_7H_5N_3O_6$)

0.18 kg (6.67161 gm-mol) Aluminum (Al)

0.405 kg (1.8235 gm-mol) RDX ($C_3H_6N_6O_6$)

0.01 kg (0.0147732 gm-mol) Wax ($C_{15}H_{31}COOC_{30}H_{61}$)

1 kg Torpex \Rightarrow 10.6079 $H_2O(l)$ + 7.57051 C(s) + 11.0614 CO + 8.14519 N_2 + 6.67161 Al(s) + 1015.25 kcal

1 kg Torpex + 23.1086 $O_2 \Rightarrow$ 10.6079 $H_2O(l)$ + 18.6319 CO_2 + 8.14519 N_2 + 3.3358 Al_2O_3 + 3811.55 kcal